Application of Laser Techniques in Combustion Environments of Relevance for Gas Turbine Studies

Lantz, Andreas

2012

Application of Laser Techniques in Combustion Environments of Relevance for Gas Turbine Studies

Doctoral Thesis

Andreas Lantz

Division of Combustion Physics
Department of Physics

Lund University

Printed at Media Tryck AB, Lund, Sweden
April 2012

Lund Reports on Combustion Physics, LRCP-153
ISSN 1102-8718
ISRN LUTFD2/TFCP–153–SE
ISBN 978-91-7473-316-7

Andreas Lantz
Division of Combustion Physics
Department of Physics
Lund University
P.O. Box 118
SE-221 00, Lund, Sweden

In memory of my mother, Barbro Lantz

Abstract

In the work presented in this thesis, different laser-based techniques were employed for measurements in different combustion devices. Laser-based techniques enable non-intrusive and in-situ measurements to be carried out, in which high spatial and temporal resolution can be obtained. Different parameters related to combustion research can be visualized, such as species concentrations, temperature, velocities and particle sizes. The combustion devices investigated can be related in one way or another to gas turbine combustion, the measurements being performed in devices ranging from laboratory-scale burners to industrial gas turbine burners.

The Triple Annular Research Swirler (TARS) is a laboratory burner that simulates the character of a gas turbine, in terms of both fuel injection and flame stabilization. Studies using planar laser-induced fluorescence (PLIF) were carried out here to demonstrate how different swirler configurations affect flame and flow dynamics and how flashback depends on different operating conditions. Simultaneous measurements of OH PLIF and of acetone PLIF were employed to visualize flame position and fuel distribution, respectively, the measurements being carried out simultaneously with velocity measurements involving particle image velocimetry (PIV).

Visualization of flame position and of fuel distribution through use of OH PLIF and acetone PLIF was applied to several industrial gas turbine burners to investigate their combustion characteristics. The measurements were performed on-site at Siemens in Finspång, in burners fueled with natural gas or with a mixture of natural gas and hydrogen. The aim of the experimental investigations was to obtain a better understanding both of the mixing of air and fuel and of the flame dynamics, knowledge of which can hopefully be used to further reduce the emission levels from gas turbines. Part of the experimental results was used for the validation of computational fluid dynamics (CFD) models, used to simulate the flow and the turbulent combustion inside the combustion chamber.

A Multi-YAG laser system which can generate a rapid burst of laser pulses, and a high-speed framing camera capable of recording sequences of up to eight images, were used to study fuel vaporization, and its consequent mixing with air, in a Jet A or biojet fueled gas turbine pilot burner under elevated pressure conditions. Fuel PLIF was used to visualize both the liquid and the gas phase of the fuel, Mie scattering being used to visualize only the liquid phase of the fuel. The liquid phase of the fuel was found, as expected, to be close to the burner nozzle and the evaporated fuel to be found a

distance downstream from the burner nozzle. High-speed OH PLIF was also employed for visualizing the flame position.

Additional work carried out included characterization of partially premixed and diffusion flames in a high-pressure vessel and burner (HPVB) using OH PLIF and PAH PLIF for the visualization of flame position and of polyaromatic hydrocarbon distribution, respectively. Flames using liquid fuels (n-heptane, n-decane and ethanol) as well as gaseous (methane) fuels were studied. The results are intended to be used as data base for kinetic mechanisms and as validation data for CFD models.

Populärvetenskaplig sammanfattning

Oberoende av vilket bränsle som används ger förbränning upphov till utsläpp av miljöfarliga gaser, såsom kväveoxider, svaveldioxider, kolmonoxid och oförbrända kolväten. Dessa ämnen bidrar till försurning, smog, växthuseffekten och kan skada ozonlagret. Även koldioxid kan anses som en miljöfarlig gas då den bidrar till den globala uppvärmningen. För att få en bättre förbränning med minskade utsläpp krävs det en djup förståelse om de komplicerade kemiska och fysikaliska processer som styr förbränningen. Man behöver till exempel veta vilka temperaturer som råder på olika ställen och för olika tidpunkter i förbränningsprocessen och vilka kemiska ämnen som bildas.

I denna doktorsavhandling har laserdiagnostik använts för att öka förståelsen om förbränningsprocesser. Laserljus består i stort sett av en enda våglängd (färg) medan vanligt ljus från till exempel en glödlampa består av ett stort antal våglängder (färger). En stor fördel med en laserbaserad mätmetod jämfört med en konventionell mätmetod är att den är beröringsfri, det vill säga man behöver inte använda ett instrument i förbränningszonen som kan störa förbränningsprocessen. Mätningar kan även göras i väldigt snabba förlopp (kortare än 10 miljarddels sekund) och små strukturer i förbränningsprocessen kan studeras (ner till nästan 10 miljontedels meter). Med lasermätmetoder är det även möjligt att få tvådimensionella bilder av fördelningen av de kemiska ämnen som bildas, vilket är viktigt vid mätningar i turbulenta förlopp som förbränning i allmänhet är. Nackdelen med lasermätmetoder är att man behöver optisk tillgänglighet till mätområdet genom fönster eller optiska fibrer, vilket gör det svårt att använda lasermätmetoder i fullskaliga förbränningsapparater. Den mätmetod som används i denna avhandling är laserinducerad fluorescens.

Laserinducerad fluorescens, LIF, är en mätmetod som kan användas för att avbilda olika molekyler som bildas i förbränningsprocessen. Laserljus med en våglängd som matchar en elektronövergång i den studerade molekylen växelverkar med molekylen och ger upphov till en ljusutsändning, så kallad fluorescens. Laserinducerad fluorescens kan appliceras på många olika molekyler då olika molekyler växelverkar med olika våglängder. Molekylen OH, som är en av de viktigaste molekylerna som bildas under förbränning används för att markera flamfronten och områden där det har brunnit. Det är även möjligt att avbilda oförbränt bränsle. Använder man ett bränsle som inte fluorescerar behöver man tillsätta ett spårämne. Spårämnet måste då vara en molekyl som har liknande egenskaper som bränslet själv. I denna avhandling har aceton använts som spårämne. LIF har i detta arbete använts för att avbilda flammans position och om-

råden med oförbränt bränsle i olika gasturbintillämpningar. Mätningar har gjorts på fullskaliga industriella gasturbinbrännare men också på en nerskalad brännare. Den nerskalade brännaren använder samma metod för att spruta in bränslet och stabilisera flamman som de fullskaliga gasturbinbrännarna. I den nerskalade brännaren har fundamentala förbränningsprocesser såsom flashback, flamutsläckning och flamstabilisering studerats. Flashback och flamutsläckning är två oönskade processer på grund av att de kan ge upphov till minskad förbränningseffektivitet och högre utsläpp av föroreningar. Resultaten visade att flamman blir mer känslig för flashback när kvoten mellan bränsle och luft närmar sig ett. Mätningarna på de fullskaliga gasturbinbrännarna gjordes i samarbete med Siemens där ett stort antal gasturbinbrännare studerades för att karakterisera förbränningen vid olika driftförhållanden. Resultaten från dessa mätningar användes till exempel för att utvärdera olika simuleringsmodeller, vilka används för att simulera förbränningen i brännkammaren.

Den information som resultaten i denna avhandling gav kommer förhoppningsvis att användas för att förbättra förbränningseffektiviteten samt att minimera utsläppen av föroreningar och miljöfarliga gaser från gasturbiner.

List of Papers

This thesis is based on the following papers, which will be referenced by Roman numerals in the text.

I. Iudiciani, P., Hosseini, S.M., Szasz, R.Z., Duwig, C., Fuchs, L., Collin, R., **Lantz, A.**, Aldén, M., and Gutmark E.J., *Characterization of a multi-swirler fuel injector using simultaneous laser based planar measurements of reaction zone, flow field, and fuel distribution*, ASME Turbo Expo, Paper GT2009-60278, 2009

II. Iudiciani, P., Duwig, C., Hosseini, S.M., Szasz, R.Z., Fuchs, L., Gutmark E.J., **Lantz, A.**, Collin, R., and Aldén, M., *Proper Orthogonal Decomposition for experimental investigation of swirling flame instabilities*, 48:th AIAA Aerospace Sciences Meeting Including the New Horizons Forum and Aerospace Exposition, Paper AIAA-2010-0584, 2010

III. Hosseini, S.M., Szasz, R.Z., Iudiciani, P., Fuchs, L., **Lantz, A.**, Collin, R., Aldén, M., and Gutmark, E.J., *Study of Flame Dynamics and Flashback Mechanism in a Gas Turbine Combustor Using Simultaneous OH-PLIF and PIV*, 46:th AIAA/ASME/SAE/ASEE Joint Propulsion Conference & Exhibit, Paper AIAA-2010-6668, 2010

IV. **Lantz, A.**, Collin, R., Sjöholm, J., Li, Z.S., Petersson, P., and Aldén, M., *High-Speed Fuel/Hydroxyl Radical Imaging in a Gas Turbine Pilot Burner*, AIAA Journal, **50**(4):971-975, 2012

V. Lörstad, D., Lindholm, A., Alin, N., Fureby, C., **Lantz, A.**, Collin, R., and Aldén, M., *Experimental and LES investigations of a SGT-800 burner in a combustion rig*, ASME Turbo Expo, Paper GT2010-22688, 2010

VI. Lörstad, D., Lindholm, A., Barhaghi, D.G., Bonaldo, A., Fedina, E., Fureby, C., **Lantz, A.**, Collin, R., and Aldén, M., *Measurements and LES of a SGT-800 burner in a combustion rig*, Accepted for publication at ASME Turbo Expo, Paper GT2012-69936, 2012

VII. Verhoeven, L.M., de Andrade Oliveira, M.H., **Lantz, A.**, Li, B., Li, Z.S., Luijten, C.C.M., van Oijen, J.A., Aldén, M., and de Goey, L.P.H., *Tar conversion in biogas by partial combustion: a numerical and experimental study of Polycyclic Aromatic Hydrocarbons in a laminar diffusion flame*, Accepted for oral presentation at the 34:th International Symposium on Combustion, 2012

Related Work

A. Tian, K., Li, Z.S., Staude, S., Li, B., Sun, Z.W., **Lantz, A.**, Aldén, M., and Atakan, B., *Influence of ferrocene addition to a laminar premixed propene flame: Laser diagnostics, mass spectrometry and numerical simulations*, Proceedings of the Combustion Institute **32**:(1) 445-452, 2009

B. **Lantz, A.**, Collin, R., Sjöholm, J., Li, Z.S., Petersson, P., and Aldén, M., *High-speed imaging of fuel/OH distributions in a gas turbine pilot burner at elevated pressure*, 49:th AIAA Aerospace Sciences Meeting Including the New Horizons Forum and Aerospace Exposition, Paper AIAA-2011-0986, 2011

C. Baudoin, E., Bai, X.S., Yan, B., Liu, C., **Lantz, A.**, Hosseini, S.M., Li, B., Elbaz, A., Sami, M., Li, Z.S., Collin, R., Chen, G., Fuchs, L., Aldén, M., and Mansour, M.S., *Effect of partial premixing on stabilization and local extinction of turbulent methane/air flames*, 7th Mediterranean Combustion Symposium, 2011

D. Nogenmyr, K.-J., Petersson, P., Bai, X.S., Fureby, C., Collin, R., **Lantz, A.**, Linne, M., and Aldén, M., *Structure and stabilization mechanism of a stratified premixed low swirl flame*, Proceedings of the Combustion Institute **33**:(2)1567-1574, 2011

E. Petersson, P., Collin, R., **Lantz, A.**, and Aldén, M., *Simultaneous PIV, OH- and fuel-PLIF measurements in a low swirl stratified turbulent lean premixed flame*, 5th European Combustion Meeting, 2011

Contents

Chapter 1

Introduction

Our daily life relies on combustion. We have internal combustion engines, for example, for powering cars, trucks, boats and other vehicles. Combustion is also used for the generation of electricity and in gas turbine engines for the propulsion of aircraft. Furnaces are commonly used for producing heat and electricity. Most of these devices make use of the energy released from the combustion of fossil fuels (coal, oil and natural gas). At present, 81% of the world's total energy supply comes from fossil fuels and only about 10% from biofuel and waste. The remaining parts include energy supply from nuclear, hydro, solar, wind sources, and the like [1]. However, since fossil fuel resources are limited, this proportion of the total is problematical. In addition, combustion has a negative impact on the environment due to the emission of NO_X, CO, SO_X and particulates, for example. These not only are toxic, but they also contribute on their own to photochemical smog, depletion of the ozone layer, acid rain and the greenhouse effect. However, the focus has recently been shifted toward another gas, carbon dioxide (CO_2) which is one of the main products of combustion. Since CO_2 is a greenhouse gas, it contributes to global warming [2]. Although we have to face the issues of the virtual elimination eventually of fossil fuels and of their negative environmental impact, fossil fuels will continue to be important in providing energy worldwide for the next few generations [3]. It is thus important not only to find alternative energy sources and alternative fuels but also improve the existing combustion technologies in terms of fuel consumption and the minimizing of pollutant formation. This involves developing gas turbines and internal combustion engines in this direction, for example. Also, in order to meet increasing global demands for energy in the coming generations, alternative fuels which do not depend on fossil fuels and that have a tolerable environmental impact need to be developed. Examples of alternative fuels are biofuel, hydrogen, alcohol fuels (ethanol and methanol) and synthetic fuels. Hydrogen is probably the closest one can come to an ideal fuel due to its high flame speed, wide burning limits, easy ignition and low degree of pollutant formation [4].

Combustion is a complex process involving a variety of physical and chemical processes taking place over a wide range of time and length scales. To fully describe the

chemical mechanisms in combustion, numerous species and hundreds of chemical reactions are required [2]. The description of the combustion in practical devices such as gas turbines and internal combustion engines is even more complex since the processes involved rely, virtually without exception, on a turbulent gas flow. Turbulence is a random process in which the fluid velocity fluctuates in terms of both time and space. Turbulent flows consist of eddies of varying size, ranging from the largest length scale (an integral length scale), of the same order of magnitude as the geometry of the flow, down to the smallest length scale (the Kolmogorov length scale), in which the kinetic energy is dissipated into heat. The largest eddies contain most of the kinetic energy of the flow. The smaller the eddies are, the lower their contribution to the kinetic energy involved [5]. In turbulent combustion, the flow velocity, the species concentration and the temperature fluctuate randomly. The convective motion of the eddies increases the transport of both heat and mass, a highly wrinkled and fluctuating flame front being found. If the flame front is too wrinkled, however, it can lead to flame quenching. In addition, the turbulence enhances the mixing of the fuel and the oxidizer, important in non-premixed flames in which the fuel consumption is controlled by mixing. However, since turbulence is a random process, it can cause combustion instabilities if it interacts with acoustic waves [6].

To be able to improve existing combustion technologies in terms of fuel consumption and of pollutant formation and to develop alternative energy sources and alternative fuels, it is necessary to increase the understanding of combustion, especially of turbulent combustion. There are different ways to increase the understanding of it, one of these being to use measurement techniques to physically measure the combustion process in different combustion environments. Measurements of this sort can be carried out using conventional probe techniques and/or laser-based techniques. Another way of increasing knowledge of combustion is to model turbulent flow and combustion, by use, for example, of CFD (computational fluid dynamics) and/or of chemical models. Numerical models need to be validated against experimental data. Accordingly, these two approaches are often used to complement each other, since experimental results can be used for the validation of the models in question.

Laser diagnostics, used in the present study, is a valuable tool in combustion research since it makes it possible to measure important parameters, such as temperature, species concentration, particle and droplet size, and flow velocity [7, 8]. It is also possible to study the mixing of fuel and air, fuel atomization and fuel vaporization, very important as they are in order to optimizing the combustion and minimizing the unwanted emissions. Laser-based techniques, in contrast to probe techniques, are usually regarded as non-intrusive, the laser radiation does not disturb the chemical or the flow dynamics of the processes that are investigated. Lasers allow remote sensing to take place, this enabling in-situ measurements to be performed in hostile environment such as gas turbines and internal combustion engines. Employing lasers makes it possible for measurements of very high spatial resolution ($\sim$10-50 µm) to be obtained and when pulsed laser sources are used, measurements of high temporal resolution (<10 ns) can be achieved. During the short periods of time involved, the combustion processes can be considered as being “frozen”. This means that measurements can be carried out faster

than the characteristic time scales of the flow field and of many of the chemical reactions involved. Another advantage of using laser diagnostics is that of being able to conduct species-selective studies in which the tunable capabilities of the laser sources enable unique spectral characteristics of the molecules to be probed. Laser-based techniques have certain limitations, however, the need of having optical access to the measurement volume being a major one. In practical combustion devices, such as in gas turbines, special designs for the mounting of quartz windows to the combustion chamber as well as various additional components are required.

The work presented in the thesis involves the use of laser techniques in efforts to improve the knowledge of combustion process in various combustion devices. The combustion devices that were investigated can be related in one way or another to gas turbine combustion. Measurements to visualize flame positions, fuel distributions and flow fields were utilized in both laboratory-scaled gas turbine model combustors and industrial gas turbine burners. The measurements involve studies of combustion processes, such as flashback, liftoff and blow-out. Increased knowledge of these is of great importance since for gas turbine combustors they are unwanted combustion events. Parts of the experimental results are also used for the validation of different CFD models, such as large eddy simulations (LES) and Reynolds-averaged Navier-Stokes (RANS) simulations. LES is a technique in which the larger eddies, which contain most of the kinetic energy of the flow, are computed explicitly, whereas the small eddies are modeled using sub-grid-scale models. In RANS, only the statistical mean field of the flow is solved, the effects of all the eddies that occur being modeled [6].

The outline of the thesis is as follows. Chapter 2 deals with the measurement techniques employed. It provides a brief introduction to the basic principle of the measurements techniques used, such as laser-induced fluorescence and particle image velocimetry. In chapter 3 the measurement equipment, in particular the laser sources and the detector used in the experimental work are described. The specific combustion devices that were investigated are presented in chapter 4, which includes a general introduction to gas turbine combustion. Chapter 5 presents a selection of examples of the applications studied and of the results obtained, including the characterization of the TARS burner, high-speed OH/fuel imaging of a gas turbine pilot burner, OH/fuel visualization measurements performed on-site on industrial gas turbine burners at Siemens in Finspång as well as measurements in a high-pressure vessel and burner (HPVB). Finally, a summary of the work and an assessment of the outlook for the future is provided in chapter 6. The published papers included in the thesis are attached at the end of it.

Chapter 2

Diagnostic techniques

The different techniques employed in the thesis work are described in this chapter. Most of the applications presented are based on the use of laser-induced fluorescence and various of the applications involve particle image velocimetry. The basic theory behind laser-induced fluorescence, which is a well established optical measurement technique for species distribution measurements, is presented in section 2.1.1. In the two sections that follow, 2.1.2 and 2.1.3, techniques for the visualization of species distributions are discussed. The particle image velocimetry technique is taken up at the end of the chapter.

2.1 Laser-induced fluorescence

Atoms and molecules can be visualized as clouds of electrons orbiting around a nucleus. The electrons are restricted to orbits with discrete energies, the different orbits building up energy levels specific to the species. Transitions between these discrete levels occur by means of photon processes, such as absorption, spontaneous emission and stimulated emission. Absorption is a process in which a photon is absorbed by the atom or molecule and an electron is excited from a lower to a higher energy level. Spontaneous emission is the process by which an electron spontaneously de-excites from a higher to a lower energy level and stimulated emission being the process by which an electron is induced by the presence of a photon to de-excite from a higher to a lower energy level. The absorption and stimulated emission processes involved require that the photon energy be equal to the energy separation between the two participating energy levels. The radiation emitted by an atom or molecule when it de-excites by spontaneous emission of a photon from a higher to a lower energy level is referred as fluorescence. In laser-induced fluorescence (LIF) processes the atom or molecule is excited to the higher energy level by use of laser excitation, the wavelength being tuned to the resonance between the two energy levels. After excitation, the upper energy level can undergo a number of successive processes. The atom or molecule can return to the lower energy level by stimulated emission induced by laser radiation. It can absorb an additional

photon and be excited to a higher energy level or even be ionized, the latter process being termed photoionization. If a molecule is involved, it can dissociate into smaller fragments or its internal energy can be altered by inelastic collisions with surrounding atoms or molecules, producing rotational energy transfer (RET), vibrational energy transfer (VET) and electronic energy transfer. A molecule can also have energy losses from the excited state due to collisions with other molecules or atoms, this leading to a non-radiative de-excitation of it. Finally, the atom or molecule can spontaneously de-excite to lower energy levels and emit photons, i.e. fluoresce. The light emitted has either the same wavelength as the excitation wavelength (resonance fluorescence) or a different wavelength. The fluorescence wavelength is usually Stokes shifted, meaning that the fluorescence occurs at a wavelength longer than the excitation wavelength. In performing LIF measurements in combustion environments, this shift is used to avoid or suppress interference from laser-scattered light. Because of the discrete energy levels, the absorption spectra and emission spectra are specific for every atom and molecule, which allows species-specific measurements to be carried out. Since the absorption process is usually resonant, the absorption cross section is large, which makes the LIF technique capable of detecting species at the ppm or sub-ppm level. The large absorption cross section also makes it possible to use LIF for 2-dimensional imaging, planar laser-induced fluorescence (PLIF). Since lasers are used for excitation, LIF features both high spatial resolution (∼10-50 μm) and high temporal resolution (<10 ns).

2.1.1 Basic theory of LIF

For describing the basic characteristics of LIF one can consider a simple two energy level model, such as diagrammed in Fig. 2.1. The energy and the population found in the lower level are E_1 and N_1, respectively, and those in the upper level are E_2 and N_2. b_{12}

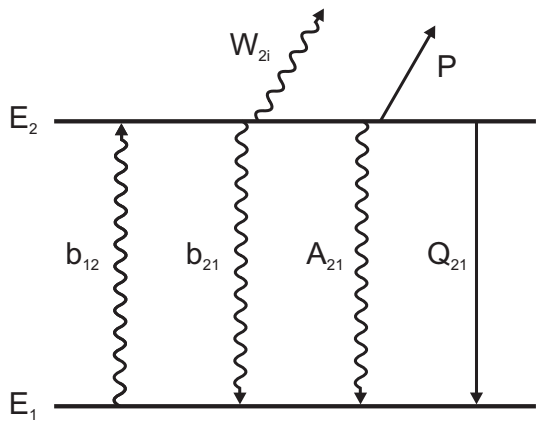

Figure 2.1: *Energy level diagram for a two-level fluorescence model.*

and b_{21} being the rate constants for absorption and stimulated emission, respectively, these being related to the Einstein B coefficient for absorption and stimulated emission through

$$b = \frac{BI_v}{c} \tag{2.1}$$

where I_v is the laser spectral irradiance and c is the speed of light. A_{21} is the Einstein coefficient for spontaneous emission, Q_{21} the collisional quenching rate constant, $W_{2\mathrm{i}}$ the photoionization rate constant and P the predissociation rate constant. The latter three rate constants, which represent non-radiative transitions, reduce the fluorescence signal. The rate equations for the populations of the two energy levels are given by

$$\frac{dN_1}{dt} = -N_1 b_{12} + N_2(b_{21} + A_{21} + Q_{21}) \tag{2.2}$$

$$\frac{dN_2}{dt} = N_1 b_{12} - N_2(b_{21} + A_{21} + Q_{21} + W_{2i} + P) \tag{2.3}$$

In general, the predissociation and photoionization rate constants are neglected, since most excited states are not predissociative and photoionization can be avoided by choosing a laser energy that is sufficiently low. With the assumption that the population of the excited state prior excitation is negligible and that the two energy levels represent a closed system with no population loss, Eqs. 2.2 and 2.3 result in

$$\frac{dN_1}{dt} + \frac{dN_2}{dt} = \frac{d}{dt}(N_1 + N_2) = 0 \tag{2.4}$$

which gives

$$N_1 + N_2 = N = N_1^0 \tag{2.5}$$

where the zero superscript identifies the initial population of level N_1 and N is the total population. Equation 2.3 has an algebraic solution if a steady-state for the processes considered in Fig. 2.1 is established and if Eq. 2.4 holds. The equation can be solved for N_2 by eliminating N_1, when the initial condition is $N_2(t = 0) = 0$, the solution then being

$$N_2(t) = \frac{b_{12} N_1^0}{(b_{12} + b_{21} + A_{21} + Q_{21})}(1 - e^{-(b_{12}+b_{21}+A_{21}+Q_{21})t}) \tag{2.6}$$

After a short period of time ($\sim$1 ns), the system reaches the steady-state for the processes shown in Fig 2.1. Equation 2.6 can then be written as

$$N_2 = N_1^0 \frac{b_{12}}{b_{12} + b_{21}} \frac{1}{1 + \frac{A_{21}+Q_{21}}{b_{12}+b_{21}}} = N_1^0 \frac{B_{12}}{B_{12} + B_{21}} \frac{1}{1 + \frac{I_{sat}^{\nu}}{I_{\nu}}} \tag{2.7}$$

where the saturation spectral irradiance I^{ν}_{sat} is defined as

$$I^{\nu}_{sat} = \frac{(A_{21} + Q_{21})c}{B_{12} + B_{21}} \tag{2.8}$$

The fluorescence rate is converted to a total fluorescence signal power F by temporal integration over the duration of the laser pulse. The fluorescence signal power, which is proportional to $N_2 A_{21}$, can be written as

$$F = h\nu N_2 A_{21} \frac{\Omega}{4\pi} lA = h\nu \frac{\Omega}{4\pi} lAN_1^0 \frac{B_{12}}{B_{12} + B_{21}} \frac{A_{21}}{1 + \frac{I^{\nu}_{sat}}{I_{\nu}}} \tag{2.9}$$

where h is Planck's constant, ν is the frequency of the emitted photon, Ω is the collection solid angle, l is the axis from which the fluorescence is collected and A is the focal area of the laser beam. The fluorescence signal is proportional to the initial population of the energy level at which the excitation takes place, which is related to the total species population via the Boltzmann distribution.

For low levels of laser irradiance, $I_{\nu} \ll I^{\nu}_{sat}$, Eq. 2.9 can be rewritten as

$$F = \frac{h\nu}{c} \frac{\Omega}{4\pi} lAN_1^0 B_{12} I_{\nu} \frac{A_{21}}{A_{21} + Q_{21}} \tag{2.10}$$

The fluorescence is said to be in the *linear regime* since the power of the fluorescence signal is linearly proportional to the laser irradiance. The fluorescence is proportional to the number of molecules of the probed species contained in the measurement volume, lAN_1^0. The term $\frac{A_{21}}{(A_{21}+Q_{21})}$ is the fluorescence quantum yield or Stern-Volmer factor. Usually, quenching is the dominant process, resulting in the fluorescence quantum yield being much smaller than unity. This means that most of the excited molecules lose their excitation energy through non-radiative processes. In order to perform quantitative measurements, the quenching rate constant Q_{21} needs to be known. Determing it is not an easy task since the quenching rate constant is a function of the pressure, the temperature, and of the molecular collisional partners. There are different approaches to obtaining Q_{21}. One approach is to measure the temperature and the major quenching species and to calculate the quenching correction needed for the data [9, 10]. Another approach is to measure the lifetime and hence the quenching rate constant [11, 12]. The lifetime, τ, is related to the quenching rate constant through

$$\tau = \frac{1}{(A_{21} + Q_{21})} \tag{2.11}$$

where A_{21} is assumed to be known. In stable flows and laminar flames, these approaches work very well since it is possible to carry out sequential and/or time average measurements. If a sufficient signal-to-noise ratio is provides, the approach in which the lifetime is measured can also be used in a turbulent environment.

A strategy for avoiding quenching corrections is to be in the *saturated regime*, the laser excitation irradiance being higher than the saturation irradiance, $I_\nu \gg I_{sat}^\nu$. In this regime, Eq. 2.9 can be rewritten as

$$F = h\nu \frac{\Omega}{4\pi} l A N_1^0 \frac{B_{12}}{B_{12} + B_{21}} A_{21} \tag{2.12}$$

Here, the fluorescence signal is independent of both the laser excitation irradiance and the quenching rate constant. In this regime the fluorescence signal is maximized, but at certain wavelengths it may be difficult to achieve a sufficiently high level of laser irradiance. Also, it can be difficult to achieve saturation in the wings of a focused laser beam and during the entire duration of a laser pulse.

Other strategies to avoid quenching corrections are predissociative LIF and photoionization LIF. In predissociative LIF the molecule is excited to a predissociative state in which $P \gg Q > A$, loss from the excited state thus being dominated by P. This approach hold at low to atmospheric pressures whereas at higher pressures $Q \approx P$, which means that the quenching cannot be neglected. Photoionization LIF is similar to predissociative LIF, with the difference that, in the former case the loss from the excited state is dominated by $W_{2\mathrm{i}}$. Photoionization there is achieved by using a second laser that overlaps the fluorescence-induced laser in the measurement volume and photoionizes the molecule. Both predissociative LIF and photoionization LIF suffer from low fluorescence efficiency and low species detectivity.

Despite the difficulties in achieving quantitative information, LIF in the linear regime is still the most applied approach when performing measurements in combustion environments. It is possible to obtain qualitative information regarding species distribution and temperature in the combustion zone. In the thesis, qualitative visualization of flame position and of fuel distribution has been utilized through use of OH PLIF and fuel PLIF, respectively.

A more thorough account of the theory behind LIF, saturated LIF, predissociative LIF and photoionization LIF can be found in a book by Eckbreth [8] and in review articles by Kohse-Höinghaus [13] and Daily [14].

2.1.2 OH LIF

One of the most important intermediate species formed during combustion is the hydroxyl radical, OH. It is formed in the reaction zone by fast two-body reactions, where two example being $\mathrm{H}+\mathrm{O}_2 \rightarrow \mathrm{OH}+\mathrm{O}$ and $\mathrm{O}+\mathrm{H}_2 \rightarrow \mathrm{OH}+\mathrm{H}$. OH is thus often used as a flame front marker, yet since the consumption of the OH radical occurs through slow three-body reactions, OH radicals are also found in post-flame regions. Because of this, the OH radical can act as a marker for both the flame front and the burnt gas regions. The OH radical is spectroscopically well characterized, the two most common excitation schemes in performing laser-induced fluorescence measurements being $A^2\Sigma^+\,(v'=0) \leftarrow X^2\Pi\,(v''=0)$ and $A^2\Sigma^+\,(v'=1) \leftarrow X^2\Pi\,(v''=0)$, where v' and v'' denotes vibrational levels in the first excited electronic state and the ground state,

respectively. Usually, the latter transition is used for excitation and the first for the collection of fluorescence light. Figure 2.2 shows a schematic excitation and fluorescence scheme of the OH radical. Directly after excitation, collisions with surrounding species lead to a redistribution of the energy level population throughout so-called rotational energy transfer (RET) as well as vibrational energy transfer (VET). These processes bring molecules from the pumped level selected to neighboring rotational and vibrational levels. The RET and VET rates are generally higher than the quenching and spontaneous emission rates. Accordingly, many different rotational levels in $v' = 0$ are populated, the fluorescence thus being emitted from several different rotational levels and its being of many different wavelengths.

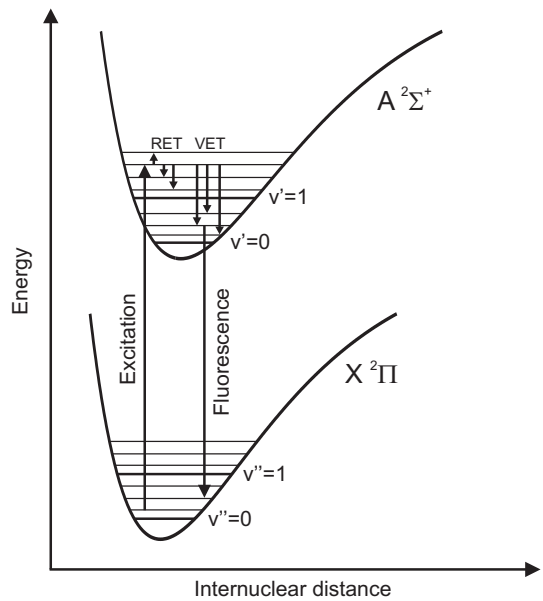

Figure 2.2: *A schematic energy-level diagram of the excitation and fluorescence scheme of the OH radical.*

In the work reported in the thesis, an Nd:YAG/dye laser system was used to excite the $Q_1(8)$ transition near 283 nm in the $A^2\Sigma^+ (v' = 1) \leftarrow X^2\Pi (v'' = 0)$ system. The $Q_1(8)$ transition was chosen because it shows strong fluorescence and is almost temperature-insensitive over the flame temperature region (1400 K to 2500 K), as can be seen in see Fig. 2.3 and in [15]. The resulting fluorescence is detected at around 308 nm, its originating from the $A^2\Sigma^+ (v' = 0) \leftarrow X^2\Pi (v'' = 0)$ band. This Stokes shift, of around 25 nm, makes it possible to effectively suppress the interference from laser-scattered light.

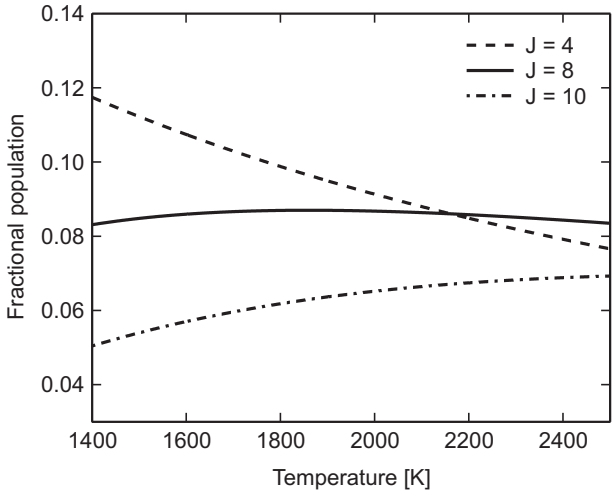

Figure 2.3: *Fractional populations of three different rotational levels ($J = 4$, 8 and 10) in the $X^2\Pi$ state as functions of temperature.*

2.1.3 Fuel LIF

In order to optimize the combustion and minimize the emissions from practical combustion devices such as gas turbines and internal combustion engines, studies of the mixing of fuel and air, fuel atomization and fuel vaporization are very important. The fuel visualization technique is a powerful tool for such studies since it yields information regarding the fuel distribution. A common strategy for fuel visualization is to excite a fluorescent tracer added to a non-fluorescing fuel. Adding a fluorescent tracer to the fuel is necessary when using methane, natural gas or other gaseous fuels that do not fluoresce when illuminated by UV radiation. There are a number of properties that the tracer which is added must fulfill. The most important of these is that the tracer needs to follow the fuel flow and be consumed in the combustion process in the same way as the fuel. Other important properties are that the tracer should generate a strong LIF signal when excited by a pulsed high-power laser, that the absorption and emission bands should be well separated and that the intensity of the fluorescence should be independent of temperature, pressure and the composition of the surrounding gas [16]. Different classes of molecules can be used as tracers, the choice of class depending upon the specific fuel used and on the combustion environment. Ketones (e.g. acetone and 3-pentanone) and aromatic hydrocarbons (e.g. benzene and toluene) are frequently used as tracers. Other possible fuel tracers are acetaldehyde and biacetyl [16, 17]. Acetone LIF is discussed in particular detail since it was used as fuel tracer in the measurements carried out in the TARS burner, Papers I and II, and at Siemens, Papers V and VI. Another strategy, which is the simplest and most straightforward one, is to use liquid multi-component fuels in so far as possible, since these fluoresce when illuminated with

UV radiation. Examples of such fuels are Jet A and biojet. These contain a variety of hydrocarbons, including long chains of carbon groups and poly-aromatic hydrocarbons. Fuel visualization measurements using Jet A and biojet are reported in Paper IV.

Acetone LIF

Acetone ($[CH_3]_2CO$) is an ideal tracer in gaseous flows due to its high vapor pressure and relatively low boiling point (56 °C), and it is used in many different applications [18–20]. At room temperature the UV absorption band of acetone extends from 225 nm to 320 nm, with a maximum at 275 nm. The resulting emission band is between 350 nm and 550 nm, with a maximum at 435 nm [21]. Its rather broad absorption band allows acetone to be excited by pulsed high-power lasers. Example of such lasers are excimer lasers, frequency-quadrupled Nd:YAG lasers and frequency-doubled dye lasers. The absorption and emission bands are spectrally separated, making it possible to avoid or suppress the interference from laser-scattered light. Other advantages in using acetone as a fuel tracer are its high fluorescence signal intensity, its short lifetime and the fact that the signal is linear proportional to laser energy [22]. The short lifetime minimizes the effects of quenching on the fluorescence yield, the strong fluorescence signal also permitting the seeding levels to be low. Normally, up to 10 vol% of the fuel is replaced by acetone.

When employing acetone as a fuel tracer in reacting flows, the temperature and pressure dependence of the fluorescence signal need to be borne in mind. Several research groups have studied these dependences for different excitation wavelengths [23–26], observing that the absorption spectra are red-shifted as the temperature increases and that the absorption cross-section increases with increasing temperature for wavelengths above 266 nm. The fluorescence intensity increases with increasing temperature for wavelengths above 266 nm and decreases for wavelengths below 266 nm. In response to an increase in pressure, the fluorescence intensity increases up to 4-6 bar, depending upon the excitation wavelength, before reaching a plateau and becoming independent of the pressure. It reaches the plateau faster for longer excitation wavelengths, making longer wavelengths preferable. In LIF applications it is thus preferable to use longer excitation wavelengths (280-320 nm) in order to minimize both the pressure and the temperature dependences of the fluorescence signal.

Liquid fuel LIF

Jet A and biojet are two commercial liquid multi-component fuels used in industry and in gas turbine applications. Both types of fuel are composed of many different hydrocarbon groups, and thus have an absorption band in the UV region, see [27] and Paper IV, which is accessible by use of standard laser systems. The emission band is between 266 nm and 400 nm. However, Jet A shows strong absorption at around 266 nm, which can be a problem for LIF measurements. The laser power can fluctuate or be completely absorbed. The best solution for avoiding absorption is to use laser wavelengths longer than 266 nm. In Paper IV, both 266 nm and 300 nm were used as

excitation wavelengths in studying this absorption effect. For 266 nm excitation, the fluorescent signal occurs between 266 nm and 400 nm, whereas for 300 nm excitation it occurs between 300 nm and 400 nm [28]. Since these fuels are not well characterized optically, it is difficult to know how the fluorescence relates to different parameters, such as temperature, pressure and quenching, and in what relations of these the different fuel components fluoresce. The content of these fuels can also differ from both batch to batch and depending on age. As a result, it is difficult to obtain quantitative measurements with use of fuels of this type, although it is possible to obtain qualitative information regarding the fuel distribution. It is also difficult to model the combustion of multi-component fuels, which makes comparison between modeling results and measured data difficult to obtain.

2.2 Particle image velocimetry

The structure and dynamics of turbulent flames are affected by many different parameters, such as local gas velocity, entrainment and large- and small-scale structures. The local gas velocity field can be studied, for example, by use of particle image velocimetry (PIV). PIV is a non-intrusive technique in which information about the velocity field can be extracted simultaneously across the entire plane of interest. However, the flow under investigation has to be seeded with small particles in order for the velocity field to be determined. The principle to be followed is to determine the velocity on the basis of fundamental properties, and to measure it in terms of the displacement $\mathbf{D}(\mathbf{X}; t', t'')$ of the seeded particles within a short time interval $\Delta t = t'' - t'$, i.e.

$$\mathbf{D}(\mathbf{X}; t', t'') = \int_{t'}^{t''} v\left[\mathbf{X}(t), t\right] dt \tag{2.13}$$

where $v\left[\mathbf{X}(t)\right]$ is the velocity of the seeded particles.

The basic principles involved in the technique are shown in Fig. 2.4. The seeded particles in the flow are illuminated by a thin light sheet, which exposes the seeded particles twice within a short time interval Δt. The most common light source for a PIV system is a double-pulsed frequency-doubled Nd:YAG laser. The laser makes it possible to "freeze" the particles without blurring them. The scattered light from the seeding particles is recorded by a CCD camera, the commonest being to record the two different exposures on separate image frames. The displacement of the particles can be obtained by dividing the images into small cells, so-called interrogation windows, and computing the cross-correlation for each interrogation window on a pixel-to-pixel basis. The velocity is then calculated using Eq. 2.13, since Δt (the time between the laser pulses) is known. Cross-correlational calculations are obtained for each interrogation window in order to build up the complete 2-dimensional velocity vector map.

Several parameters, such as the thickness of the laser sheet, the time separation between the laser pulses, the choice of seeding particles and the size of the interrogation windows, need to be optimized for suitable accuracy and quality of the velocities that

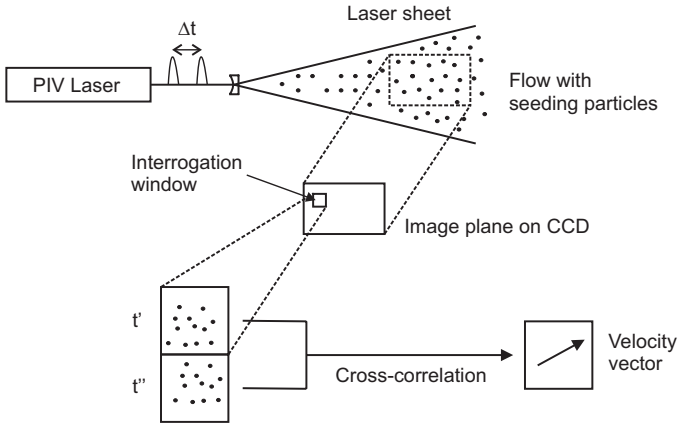

Figure 2.4: *Basic principles of the PIV technique.*

are to be obtained. The thickness of the laser sheet is usually in the order of 0.5-2 mm and is chosen in relation to the flow velocity perpendicular to the laser sheet. The time separation between the laser pulses needs to be long enough to make it possible to determine the displacement between the images of the seeded particles, and at the same time short enough to avoid particles with out-of-plane velocity components leaving the laser sheet during the period between the two exposures. For accurate measurements to be obtained, the size of the seeding particles needs to be small enough that the response time of the particles to the motion of the fluid is reasonably short, enabling the flow to be followed accurately, yet large enough to scatter sufficient quantities of the laser light. The seeding particles used in gaseous flows have a mean diameter in the order of 1-10 μm. The size of the interrogation windows determines the spatial resolution, since a separate velocity vector is calculated for each interrogation window. Thus, the interrogation windows need to be small in size in order to resolve small structures satisfactorily, yet be large enough to contain a sufficient number of particles for the velocity to be accurately determined. For good results, the number of seeded particles within an interrogation window needs to be approximately fifteen [29].

PIV can be combined with other optical techniques, for instance, it can be combined with PLIF to study interaction between flames and flowfields [30, 31]. In the measurements reported in Papers I-III, PIV was combined with PLIF for studies of flow and flame dynamics in a turbulent swirling flame. A more extensive description about PIV can be found, for example in [29, 32, 33].

Chapter 3

Measurement equipment

In this chapter the equipment most frequently used in the experiments is described, such as lasers and detectors. First, in section 3.1, a general description of lasers is provided, including a detailed discussion of the two lasers used in this work: the Nd:YAG laser and the dye laser. For a more detailed account of lasers, the reader is referred to books written by Svelto [34] and Siegman [35]. In section 3.2, the detector used for the most part in this work is described. At the end of the chapter, in section 3.3, a description of both a high-speed laser system and of a camera system used in Paper IV is provided.

3.1 Laser

Laser (Light Amplification by the Stimulated Emission of Radiation) is an optical source that emits photons in a coherent beam. A laser consists of an active medium, placed between two mirrors that form a cavity, see Fig. 3.1. One of the mirrors is highly reflective and the other is partially transmissive in order to transmit the laser light that is generated. The active medium consists of solid crystals, liquid dyes, gases or semiconductors. It can be stimulated to emit photons when external energy is applied, such as by a flash lamp or another laser source.

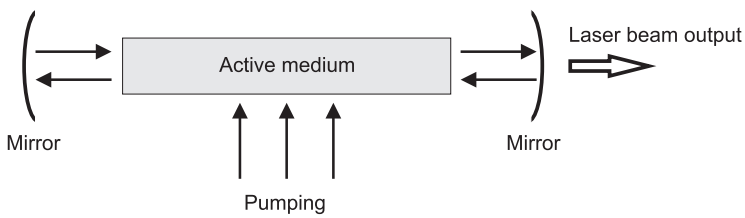

Figure 3.1: *Schematic sketch of a laser cavity. The laser-active medium is placed between two mirrors that form a cavity. One of the mirrors is highly reflective and the other is partially transmissive in order to transmit the laser light.*

In stimulated emission, an incoming photon with an energy corresponding to the difference between two energy levels involved, induces the emission of a second photon. This photon has same phase and wavelength, and travels in the same direction, as the incoming photon. The amplification of light thus obtained forms the basis of laser action. For stimulated emission to occur in the active medium, there need to be more atoms in the upper than in the lower energy level. This is referred as population inversion. It is not possible, however, to create a working laser based on absorption and emission between only two energy levels. Since the rate at which the upper level is populated by absorption equals that at which atoms leave by stimulated emission, the best one can hope for in a two-level system is either an equality of populations in the upper and lower levels or a state of saturation. Accordingly, in laser systems three or four energy levels are needed. In a three-level system (Fig. 3.2a), atoms or molecules are pumped into the highest of the three energy levels (E2), called the pump level. From there, spontaneous de-excitation occurs to an energy level (E3) that should be metastable. This results in this latter energy level having a long lifetime, and population inversion between the energy levels E3 and E1 being obtained. Laser emission occurs between the metastable energy level (E3) and the ground state (E1). An improvement of this behavior is obtained by use of a four-level system (Fig. 3.2b) in which the laser transition takes place between the second (E3) and first excited (E4) states. A rapid de-population of the lower laser level is needed in order to ensure that the upper level is always full and the lower level is always empty.

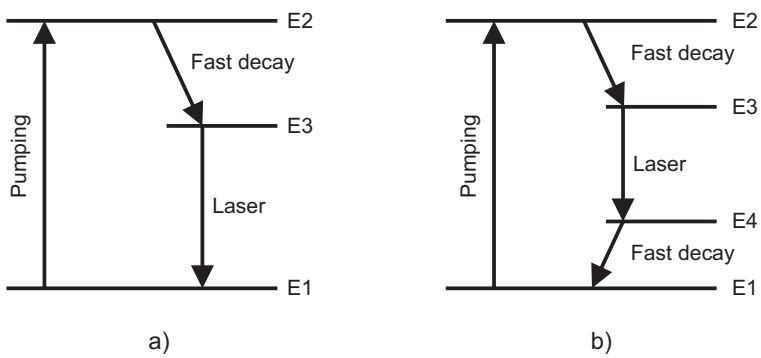

Figure 3.2: *(a) Energy level diagram of a three-level laser system. (b) Energy level diagram of a four-level laser system.*

Placing the active medium between two mirrors, which form a cavity, leads to the stimulated photons oscillating back and forth and their being amplified each time they pass through the active medium. One of the mirrors is partially transmissive, its letting through a small amount of the coherent beam, which is the laser beam. Laser beams have unique properties compared with other light sources. For instance, laser radiation is concentrated in a narrow range of wavelength. Laser radiation is also coherent, both in space and time, and is collimated, since all the photons travel in the same direction.

3.1.1 Nd:YAG laser

The Nd:YAG laser is one of the most frequently employed high-power pulsed solid state lasers. It is used either directly, such as in fuel visualization [36], formaldehyde visualization [37], laser-induced incandescence [38] and PIV and Raman spectroscopy [39], or as a pumping source for dye lasers or Ti:sapphire lasers.

The host medium in Nd:YAG lasers is a yttrium aluminium garnet ($Y_3Al_5O_{12}$) crystal in which some of the Y^{3+} ions are replaced by neodymium Nd^{3+} ions. The active lasing medium is composed of the Nd^{3+} ions and the laser functioning as a four-level laser. A simplified energy level diagram of it is shown in Fig. 3.3. The two primary absorption bands for Nd:YAG lasers are at 730 nm and 800 nm, respectively. The Nd^{3+} ions are excited to higher energy levels, E_2, through optical pumping, usually by use of a flash lamp. Following this excitation, electrons are rapidly coupled through fast non-radiative decay to a lower metastable state E_3 ($^4F_{3/2}$). From this state, further de-excitations to lower levels E_4 ($^4I_{11/2}$, $^4I_{13/2}$ and $^4I_{15/2}$) occur. The $E_3 \rightarrow E_4$ transition is forbidden via the electronic dipole transition but is weakly allowed on the basis of crystal-field interaction, the relaxation rate thus being slow (approximately 230 μs). Because of this relatively long period of time, a marked population inversion is built up in the $^4F_{3/2}$ level by the flash lamp, this level thus serving as the upper level in laser radiation. Several laser transitions are possible, either between $^4F_{3/2}$ and lower exited levels ($^4I_{15/2}$, $^4I_{13/2}$ and $^4I_{11/2}$) or between $^4F_{3/2}$ and sublevels in the ground state, $^4I_{9/2}$. The strongest transition is the $^4F_{3/2} \rightarrow {}^4I_{11/2}$ transition, the energy emitted by it having a wavelength of 1064 nm. This is the most frequently used lasing wavelength

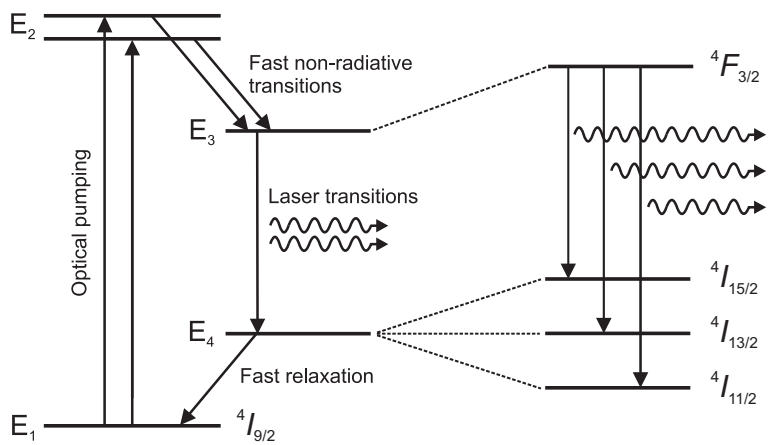

Figure 3.3: *Schematic energy level diagram of a four-level laser including relevant transitions for the Nd:YAG laser. The optical pumping is done by flash lamps at two absorption bands, at 730 nm and 800 nm, respectively, the lasing at 1064 nm occuring between the $^4F_{3/2}$ and $^4I_{11/2}$ states.*

for Nd:YAG lasers. Level $^4I_{11/2}$ is then coupled, through a rapid relaxation, to the ground level E_1, so that thermal equilibrium between these levels is rapidly established.

A large population inversion in the active laser medium can be created by limiting the buildup of stimulated emission radiation inside the cavity. This can be performed by a technique called Q-switching. The term Q-switching comes from the fact that it involves switching the cavity Q factor from a low to a high value. The Q factor of a cavity is a measure of the ratio of the radiation energy stored in the cavity to the power loss involved. Here, an attenuator is placed inside the cavity to initially block the light path between the mirrors, this creating a large population inversion in the active medium, the Q factor for the cavity thus being low. As long as the attenuator blocks the light path, large gains are built up (the Q factor decreases), and when the attenuator is removed (the Q factor increases), intense lasing builds up very rapidly because of the high gain. This leads to generation of highly intense lasing during a very short period of time. Laser pulses produced in this way can have a peak power of 10^8 W and a pulse width of about 10 ns [40]. There are several methods of achieving Q-switching. Rotating prisms, electro-optical shutters, acousticooptical switches and saturable absorbers are a few examples of this. The different methods employed can be divided into two categories, active and passive Q-switchers, depending on whether or not some active external operation needs to be applied to the device so as to produce the Q-switching. Most Nd:YAG lasers use an electro-optical method to Q-switch. Here, a Pockels cell is placed inside the laser cavity. A Pockels cell has different polarizing and polarization-rotating elements. If a high voltage pulse is applied to the cell, it changes the polarization rotation of the cavity radiation into a loss mode. This leads to the formation of intense and short laser pulses. It is possible to determine accurately when to release the laser pulse by means of Q-switching because of the rapid response of the Pockels cell.

The fundamental output wavelength of the most widely used Nd:YAG laser is 1064 nm. This wavelength can be frequency doubled by use of a non-linear crystal so as to obtain radiation in the green region of the visible spectrum at 532 nm. This process, which is called second harmonic generation, has an efficiency of about 40-50%. Higher harmonics, third (355 nm) and fourth (266 nm), can be obtain by introducing additional non-linear crystals. The laser radiation at 532 nm and 355 nm can be profitably used to pump dye lasers so as to reach additional wavelength regions.

In the present work, the different Nd:YAG lasers employed either have pump dye lasers or are used directly in the PIV measurements. A Spectra Physics Quanta-Ray PRO-290, a Continuum NY82 and a Quantel YG980 were each of them used for pumping dye lasers, whereas a Gimini-PIV laser was used for the PIV measurements.

3.1.2 Dye laser

Most solid state lasers, such as Nd:YAG lasers, can only emit light at fixed wavelengths, due to the discrete energy levels of the active medium. Large molecules can emit light at a far greater number of wavelengths due to the different vibrational-rotational energy states found within a given electronic state. Organic dye molecules, which consist of

complex structures of polyatomic molecules, show both broad absorption and fluorescence spectra. Thus, the active lasing medium in a dye laser is an organic dye solution.

A simplified energy level diagram of a dye laser is shown in Fig. 3.4. Dye lasers are usually pumped optically by a flash lamp or by another laser. The excitation of the organic dye molecule from thermally populated rovibronic levels in the S_0 ground state to rovibronic levels in the excited S_1 state takes place in accordance with the Franck-Condon principle. Induced by collisions, the molecule is then coupled via fast (approximately 100 fs) non-radiative decays to the lowest vibrational level of the excited S_1 state. This state is depopulated by spontaneous emission into several different rovibronic levels of the S_0 state, once again according to the Franck-Condon principle. Finally, the molecule returns to the lowest vibrational level of the S_0 state by another fast (approximately 100 fs) non-radiative decay.

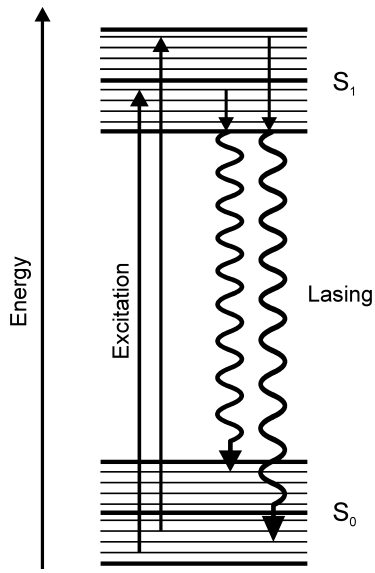

Figure 3.4: *Schematic energy level diagram of a typical dye molecule. Inspired by [8]*

The closely spaced rovibronic levels found in organic dyes are broadened to such an extent that the different fluorescence lines completely overlap. Accordingly, the absorption and fluorescence spectra consist of a broad continuum, which gives dye lasers their tunability. A dye laser can be tuned over a broad range of wavelengths ($\Delta\lambda$ = 30-50 nm). Narrowband output radiation can be generated by using a grating instead of one of the mirrors in the dye laser cavity. Use of different organic dyes enables dye lasers to operate within a broad region of wavelengths (approximately 320-1200 nm). The output wavelength can be frequency doubled and mixed by use of a non-linear crystal so as to obtain radiation in the UV spectral region.

In the work presented in the thesis, Nd:YAG/dye laser systems were employed for

performing PLIF measurements on OH radicals. The same type of dye laser, a Continuum ND60 dye laser, was used for the OH PLIF measurements in Papers I-III and V-VII. Here, a dye solution of Rhodamine 590 and methanol or ethanol was used to generate laser radiation at 567 nm. This wavelength was frequency doubled to the desirable absorption wavelength of 283 nm through second harmonic generation.

3.2 Detector

Different detectors can be used for the collection of laser-induced signals, for point measurements a Photomultiplier Tube (PMT) often being employed, a Charge Couple Device (CCD) or a Complementary Metal Oxide Semiconductor (CMOS) being used for 2-dimensional measurements. The work within the framework of the thesis was conducted by use of image-intensified CCD (ICCD) cameras. The basic operation principle of an ICCD camera is shown in Fig. 3.5.

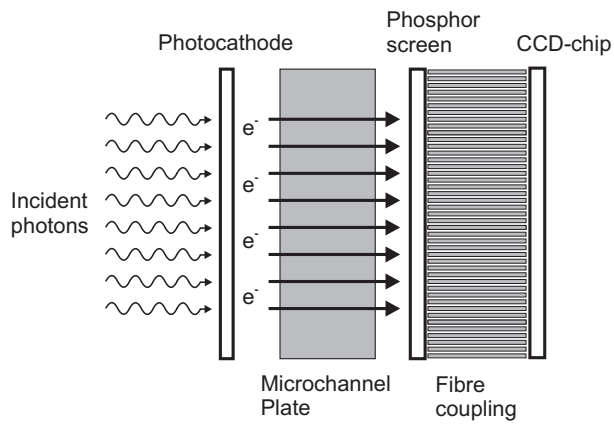

Figure 3.5: *Schematic drawing of the basic principle of an ICCD camera.*

The fluorescent light is focused onto a photocathode that converts the incoming photons to electrons. The electrons are then accelerated and amplified in a microchannel plate (MCP), which consists of several narrow channels. The high voltage applied across the MCP forces the electrons to hit the walls of the channels. This leads to the generation of secondary electrons, an avalanche of electrons being created. A multiplication factor of 10^4 along the channel in its entirely is possible. After leaving the MCP, the electron cloud hits a phosphor screen that converts the electrons to photons again. The photons are then transferred by either a fibre-coupling or a lens system onto the CCD-chip, where they are read out. The CCD acts as an integrating device, holding the image information in a matrix of separate pixels. The size of each pixel is typically around 20 µm $\times$ 20 µm. Each pixel is formed on a semiconducting substrate having a p- and an n-layer, an insulating oxide layer and metal conductors on the surface. A

small voltage is applied, generating an electric field in the semiconductor. The incoming photons produce electron-hole pairs in the p-n-junction, the electrons moving toward the minimum level in the electric field. The number of electrons is accumulated during the exposure time, the photo-electron charge of each pixel being read out to a computer.

A good feature of an ICCD is that the high voltage which is applied over the MCP can be pulsed rapidly, the detector in its entirely being gated so as to have exposure times in the nanosecond range. This operation can effectively reduce background luminescence when performing measurements in combustion environments, if nanosecond laser pulses are employed. Another nice feature is that of its being possible to detect weak signals due to the amplification stage present in the MCP. In addition, the intensity response of an ICCD detector is approximately linear, since the intensity of a pixel is proportional to the number of electrons stored.

When a CCD image is taken, noise appears togehter with the main CCD image. The three primary components of noise in a CCD imaging system are photon noise, dark noise and readout noise.

- *Photon noise* is the noise associated with the random arrival of photons at the detector. Since each photon is an independent event, the arrival of a photon cannot be predicted exactly, the probability of its arrival within a given time period being governed by a Poisson distribution. The uncertainty regarding the number of photons that will be detected during a given period of time is given by

$$\Delta N_p = \sqrt{\eta N_p} \tag{3.1}$$

  where η is the quantum efficiency and N_p is the number of photons.

- *Dark noise* arise from statistical variations in the number of electrons thermally generated within the CCD. It is independent of the photon-induced signal, but is dependent upon the temperature of the CCD. The dark noise follows a Poisson distribution, its uncertainty during a given period of time being given by

$$\Delta N_t = \sqrt{N_t} \tag{3.2}$$

  where N_t is the number of electrons that are thermally generated. The dark noise can be reduced by cooling the CCD. CCD cameras are usually cooled down to a temperature at which the dark current during the exposure time is negligible.

- *Readout noise* is generated by the CCD when the data from the chip is transferred to the computer. The major component of readout noise arises from the on-chip preamplifier, this noise being added uniformly to each image pixel. The uncertainty is given by

$$\Delta N_r = N_r \tag{3.3}$$

  where N_r is the number of readout electrons.

The signal-to-noise ratio (SNR) is usually made use of in characterizing the quality of a measurement. It is given by:

$$\mathrm{SNR} = \frac{S}{\sqrt{(\Delta N_p)^2 + (\Delta N_d)^2 + (\Delta N_r)^2}} \tag{3.4}$$

where S is the detected signal and ΔN_p, ΔN_t and ΔN_r are the photon noise, dark noise and readout noise, respectively. It is necessary to ensure that the SNR is sufficient to allow accurate image information to be obtained. There are several methods of increasing the SNR. Accumulating multiple frames or group pixels together, binning, are two ways by which the readout noise can be minimized. The detected signal increases with longer exposure times, although at the same time long exposure times result in an increase in photon noise. Different generations of ICCD cameras from Princeton Instruments, as well as a LaVision Flamestar II F camera, were employed in obtaining the PLIF measurements and a LaVision FM3S double shutter CCD camera were employed in the PIV measurements.

In addition to the PLIF measurements, a high-speed camera, Phantom V7.1 (Vision Research), was employed for chemiluminescence measurements. The high-speed camera features an 800×600 pixel SR-CMOS monochromatic sensor and has a repetition rate of 4.8 kHz at full resolution. The repetition rate can reach 10 kHz at a resolution of 512×384 pixels. The camera can also be optionally equipped with a gated image-intensifier (Hamamatsu) so as to enhance its sensitivity and enable UV detection to take place.

3.3 Multi-YAG laser and framing camera

The special Multi-YAG high-speed laser and camera system used in Paper IV is briefly described in this section. A more detailed account of the system can be found in [41], for example.

The high-speed laser system consists of four individual flashlamp-pumped Nd:YAG lasers combined into a single system (Thales). The Nd:YAG lasers operate at a repetition rate of 10 Hz and at the fundamental wavelength of 1064 nm. The four laser beams are combined and frequency doubled in a common frequency-doubling and beam-combining setup, where a laser radiation of 532 nm being generated and the separate beams being spatially overlapped. It is also possible to add a fourth harmonic crystal so as to generate laser radiation at 266 nm. The lasers can be operated in a double-pulsed mode, the Q-switch thus being open twice during a single flashlamp discharge, making it possible to obtain up to eight laser pulses. The time separation between the two pulses within a given laser can be adjusted to between 25 µs and 145 µs. The lower and upper limits are due to the gain build up time and to the length of the flashlamp discharge, respectively. Interleaving the pulses from the four lasers enables the time separation to be as short as 6.25 µs. If the four lasers are operated in a single-pulse mode, the time between two pulses can be arbitrarily set to anywhere between 0 and 100 ms. In the

measurements presented in Paper IV, the lasers were running in double-pulsed mode, the time separation between two consecutive pulses being set to 145 µs.

A high-speed framing camera (Imacon 468, Hadland) was used to detect the signals generated by the laser pulses from the Multi-YAG laser. The high framing rate was achieved by exposing eight different ICCD modules in a sequence synchronized with that of the laser pulses. Each CCD had 576×385 pixels, the signals being digitized to 8 bits. The exposure times, gains and trigger delays for each CCD could be set individually, enabling a recording rate as high as 100 MHz to be employed.

Chapter 4

Combustion devices

This chapter provides an overview of the different combustion devices that were investigated and studied in the thesis. Since the combustion devices that were studied can be related in one way or another to gas turbine combustion, a general introduction to gas turbines is presented in section 4.1. A more thorough account of gas turbines can be found in books by Lefebvre and Ballal [4] and Walsh and Fletcher [42]. The following sections (sections 4.2-4.4) describe the combustion devices investigated in the thesis. For more thorough information regarding the experimental work, including a discussion of the experimental setup and the results, the reader is directed to chapter 5.

4.1 Gas turbines

Gas turbines are used in many applications, a few example of these being aircrafts, naval ships and heat- and power-generation systems. A gas turbine consists essentially of three main parts: a compressor, a combustor and a turbine. The working principle of a gas turbine can be explained as follows. Air is compressed to high pressure in the compressor part and then enters the combustor (or combustion chamber), where it is mixed with fuel, resulting in combustion. The hot exhaust gases that are produced expand through the turbine section, where part of their energy is used to mechanically drive the compressor. The remaining energy available from the exhaust gases can be used, for example, to generate electricity for a land-based gas turbine or to generate thrust for a jet aircraft.

Gas turbines can operate in either premixed or non-premixed modes, depending on how the fuel and the air are mixed. Non-premixed combustors have the advantage of providing more stable and more easily controllable combustion than premixed combustors, but they have drawbacks in terms of pollutant emission levels. Since for non-premixed flames the combustion occurs under close to stoichiometric conditions, the flame temperature is high, this giving rise to high NO_X emission levels. In addition, soot formation is enhanced due to the presence of fuel-pockets in the hot regions. Such drawbacks can be avoided by using premixed flames, but one then has to deal with

other difficulties, such as flame blow-out [43], flashback [44] and thermo-acoustic oscillations [45]. The key problem in using premixed combustion is that to ensuring low emission levels and stable combustion at all loads [4].

Gas turbine engines have various advantages compared with other power generation systems. The major advantages are their high power-to-weight ratio and their low levels of emissions of soot and other gaseous pollutant species. In addition, the level of efficiency is high and such engines are fuel-flexible in the sense that a wide range of fuels can be used during continuous combustion [4, 46]. The efficiency can be $\sim$55 % if the hot exhaust gases heat up water in a steam boiler that serves as a steam generator. However, the efficiency can be as high as $\sim$95 % when the steam generator is used for district heating. The major drawback in the use of gas turbine engines is that, at intermediate loads, both the power and combustion efficiency are poor. The amount of air to be conveyed to the combustion chamber and the amount of fuel to be used are determined by the balance between the compressor and the turbine. At full load, this balance is optimized for high efficiency. For lower loads, further away one is from the point of the optimization, lower the efficiency of the compressor and the turbine is. The mass flow of the fuel needs to be reduced in order for the compressor and the turbine to be able to deliver less than full loads. This leads to a lower flame temperature. When the flame temperature approaches the blow-out limit, the pilot flames needs to be increased so as to avoid flame quenching. The lower the flame temperature is, the more difficult is it for the pilots to prevent flame quenching, not all of the fuel being burned under such conditions. This explains the poor combustion efficiency at intermediate load levels.

4.1.1 Emissions

The exhaust from a gas turbine is composed of pollutant gases such as NO_X, CO and unburned hydrocarbons (UHC). These gases are not only toxic, but they also contribute to photochemical smog, depletion of ozone, acid rain and the greenhouse effect [2]. Carbon dioxide, CO_2, which is one of the main products of combustion, can also be regarded as a pollutant since it contributes to global warming. The levels of concentration of the pollutants are related to factors of temperature, time and concentration histories of the combustion process. Figure 4.1 shows how the formation of CO and NO_X is affected by the flame temperature.

The formation of NO_X is highly dependent upon the temperature in the combustion zone, since the dominant form of production is through thermal NO_X formation, which is highly dependent upon the temperature, consequently NO_X is produced in high-temperature regions of the flame and post-flame gases. Above around 1900 K the rate of formation of it is especially high, resulting in a very high level of NO_X emission, see Fig. 4.1. Other mechanisms that produce NO_X are fuel NO_X and prompt NO_X. In the fuel NO_X mechanism, fuel-bound nitrogen is converted to NO_X. The amounts of fuel NO_X in gaseous fuel are very small, since the latter contains very little nitrogen, but they are higher in biofuels. In the prompt NO_X mechanism, NO_X is produced by either the CN or the HCN reaction pathway being followed. The NO_X

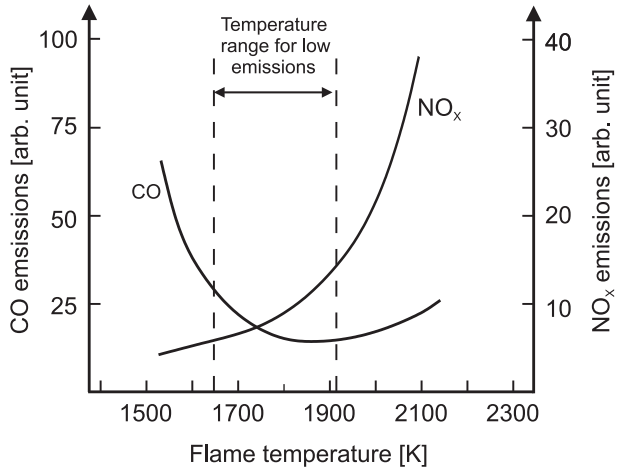

Figure 4.1: *A diagram showing the effects of the flame temperature on CO and NO_X emissions. Large amounts of CO are produced at temperatures below 1650 K, whereas the amount of NO_X increases with temperature. Thus, low emissions of CO and NO_X can only be achieved within a narrow range of temperatures. Adapted from [4]*

being found in the flame region very early and it is appearing at all temperatures. This process can be a significant contributor to NO_X emissions under lean conditions in which the temperature is low and the level of thermal NO_X formation is low as well. The most effective way of minimizing the amount of NO_X present is thus to reduce the maximum temperature in the combustion zone. This can be achieved by having either fuel-rich or fuel-lean combustion, the flame temperature in both cases being low. On the other hand, at too low flame temperature the production of carbon monoxide (CO) increases (see Fig. 4.1). CO is formed mainly under fuel-rich combustion conditions, due to the lack of sufficient oxygen there to complete the reaction to CO_2. Yet, CO can also be formed under fuel-lean combustion conditions. The low flame temperature there slows down the rate of oxidation of CO to CO_2. An increase in flame temperature increases the rate of oxidation, leading to a decrease in CO formation. However, at flame temperatures above around 1900 K, the production of CO by the dissociation of CO_2 becomes significant, this explaining why the CO emission increases at high temperatures (see Fig. 4.1).

Since large amounts of CO are formed at temperatures lower than around 1650 K and large amounts of NO_X are formed above around 1900 K, low emissions of both CO and NO_X can only be achieved within a rather narrow range of temperatures (see Fig. 4.1). Thus, it is a goal within gas turbine combustor development to achieve flame temperatures within this interval. An account of different low-emission combustor designs can be found in [4, 46], some of them being briefly described here.

- In *staged combustion* the combustion zone is divided into two zones, for example a pilot zone and a main zone, each having its own fuel nozzle. Under partial loading conditions the pilot zone is dominant and the main zone can be inactive, whereas under full load conditions the main zone is dominant. Staged combustion enables the combustor to operate over the entire power range while at the same time keeping temperatures in the combustion zone within the low NO_X- and CO-emission range. Depending upon how the zones are arranged, staged combustion can be classified as representing either *radial* or *axial* staging.

  In *radial staged combustion*, Fig. 4.2a, the two zones are located at radial positions that differ from one another and features the use of a dual-annular combustor. The major advantages of radial staging are that the length of the combustor is not greater than in the case of conventional combustors and that the two fuel nozzles can, if conditions permit, be mounted on a common feed arm. The major drawback of radial staged combustion is the poor lean blow-out limit associated with it, due to the main combustion zone and the pilot zone being isolated from one another. In addition, the temperature distribution at the outlet is altered.

  In *axial staged combustion*, Fig. 4.2b, the two zones are located at different axial positions in the combustor. The advantage of such an arrangement is that the lean blow-out limit is extended, since the hot burnt gases from the pilot zone flow through the main combustion zone. This also increases the combustion efficiency as compared with radial staged combustion. The temperate at the outlet is also more uniform. However, the combustor length is greater and the fuel nozzles need to be fed separately.

- *Lean, premixed, prevaporized (LPP) combustors*, Fig. 4.2c, involve the premixing of fuel and air upstream relative to the combustion zone. LPP combustors operate at close to the lean blow-out limit so as to lower the flame temperature and minimize the NO_X emission levels. If gaseous fuels are employed the level of soot formation is low. However, the relatively long time required for liquid fuel evaporation and fuel-air premixing upstream of the combustion zone to take place can lead to autoignition or flashback.

- In *Rich-burn, Quick-quench, Lean-burn (RQL) combustors*, Fig. 4.2d, the fuel-air mixture in the primary combustion zone is a rich one as compared with LPP combustors. The fuel-rich combustion in the primary zone enables a more stable combustion than in the case of LPP combustion to take place and the NO_X formation to be lower due to the low flame temperature. The hot product gases from the primary zone pass through a narrow passage in which additional air is injected so as to quickly quench the reactions and to produce a lean mixture. Combustion is then completed in the secondary zone under fuel-lean conditions. In the rich zone, the equivalence ration is between 1.2 and 1.6, whereas in the lean zone it is between 0.3 and 0.7. A major need in connection with the RQL method is that of achieving a near instantaneous quenching of the hot gases so as to avoid high temperatures in the secondary zone. Another problematic matter

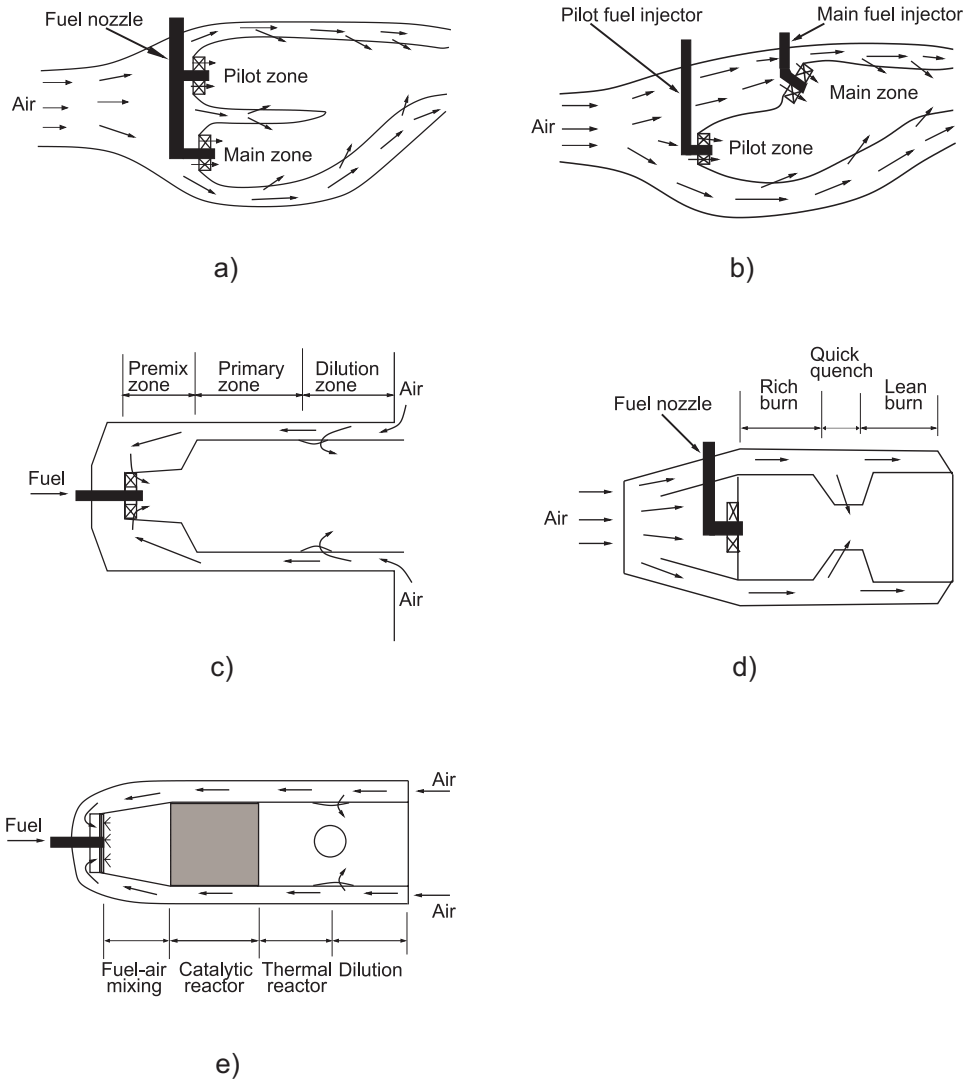

Figure 4.2: *Schematic diagrams of different low-emission combustors. (a) A radially staged combustor. (b) An axially staged combustor. (c) A Lean Premixed Prevaporized (LPP) combustor. (d) A Rich-burn, Quick-quench, Lean-burn (RQL) combustor. (e) A catalytic combustor. Inspired by [4, 46]*

is that the fuel-rich combustion in the primary zone can lead to the formation of large amounts of CO and soot.

- In *catalytic combustion*, Fig. 4.2e, low gas temperatures are obtained through oxidizing of the fuel in a catalyst. The fuel is vaporized and is mixed with air in the premixing zone before the mixture enters the catalyst where it oxidizes. The catalyst enables stable combustion to be obtained at temperatures about 1000 K lower than for conventional combustors, resulting in low NO_X emission levels and in the CO and unburned hydrocarbon emissions being low as well through both of latter being oxidized in the catalyst. One problem connected with catalytic combustion, however, is the tendency for auto-ignition of the fuel upstream of the catalyst to occur.

4.1.2 Combustor types

Depending on the shape of the combustion chamber, gas turbine combustors can be classified into tubular (or can) and annular combustors. In tubular combustors each burner has its own combustion chamber, whereas for annular combustors the burners have a common combustion chamber. Annular combustors are often selected for applications because of their compactness, lower weight, increased volume-to-surface area and tangentially smoother turbine inlet temperature distribution as compared with tubular combustors. Tubular combustors have the advantage, however, of easy maintainability. The Siemens SGT-750 [47] and the Siemens SGT-800 [48] are examples of gas turbines having tubular and annular combustors, respectively.

4.1.3 Flame stabilization

In gas turbine combustors it is important to have stable flames, since such flames are resistant to flashback, liftoff and blow-out. There are two common methods of maintaining and stabilizing the flames in a combustor: through use of a bluff body or through use of swirl (see Fig. 4.3).

A bluff body is an object of non-streamlined shape located inside the combustion chamber. An incoming fluid creates an adverse pressure gradient in the wake of the bluff body, due to the inability of the fluid to follow a non-streamlined object. This creates a recirculation zone downstream from the bluff body. This recirculation zone, which consists of hot burnt gases, helps to hold the flame at the edges of the bluff body. Flame stabilizers of this type are usually employed in ramjet and turbojet afterburner systems.

Flame stabilization by swirl is based on the presence of a central recirculation zone (CRZ) downstream from the nozzle, a zone created at a sufficiently high swirl level of the air-fuel mixture. The CRZ is created by aerodynamic means, the incoming mixture being given a swirling motion as the swirling jet expands in a radial direction, an adverse pressure gradient being created in the centerline. If the swirl is strong enough, a reversed flow is created in the center, resulting in a CRZ. An outer recirculation zone

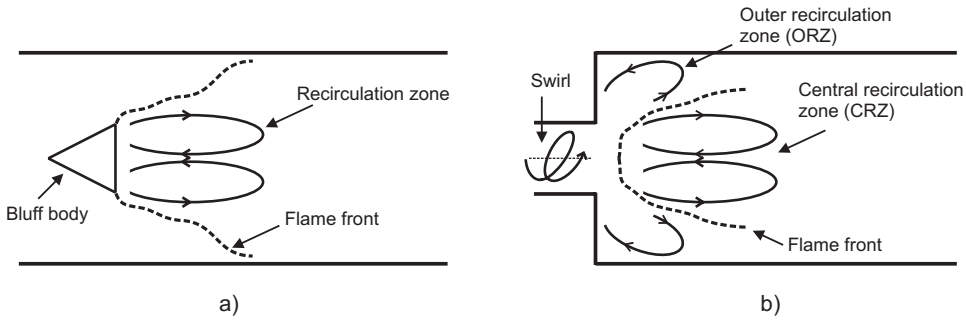

Figure 4.3: *(a) Flame stabilization by a bluff body. (b) Flame stabilization by swirl.*

(ORZ) is also created along with the CRZ. It is formed through the sudden expansion that occurs in the radial direction and the presence of the combustor walls. The different recirculation zones help to stabilize the flame. The residence time of the air-fuel mixture in the combustion chamber is increased since the axial velocity is reduced and the hot product gases will re-ignite the eventually quenched flame and preheat the air-fuel mixture. However, for the flame to be stabilized the turbulent flame speed has to be less than the gas velocity in order to prevent a flashback from occurring, while at the same time it should be higher than the average flame velocity in the combustion chamber so as to avoid the occurrence of liftoff or of a blow-out. Swirl-stabilized flames are usually employed in gas turbine combustors due to the swirl stabilization improving the air-fuel mixing and limiting the size of the flame.

4.2 TARS burner

Gas turbines operate at high Reynolds numbers (Re 10^6) and have complex geometries that provide limited optical access. Studying gas turbines by use of advanced experimental and numerical techniques is thus very difficult. One way of overcoming this is to study laboratory-scaled gas turbine model combustors that have a more simplified geometry, one example of this being the Triple Annular Research Swirler (TARS). This is a generic burner that simulates the character of a gas turbine burner, both in terms of fuel injection and of flame stabilization. The injector is one developed by Delevan Gas Turbine Products (a division of the Goodrich Corporation) in collaboration with General Electric Aircraft Engines. The swirler features three air passages, each with an individual swirler. Planar cuts of the TARS injector are shown in Fig. 4.4. The inner and the intermediate swirlers are axial swirlers, whereas the outer swirler is a radial swirler. Different configurations can be achieved by changing the different swirling vanes or directions of rotation of the swirlers. The total length of the TARS burner is 66 mm and the diameter of the outer swirler is 50.8 mm.

The TARS burner is mounted on top of an atmospheric combustion test rig. The rig consists of an inlet flange, a flow conditioning chamber (609.6 mm long) and a

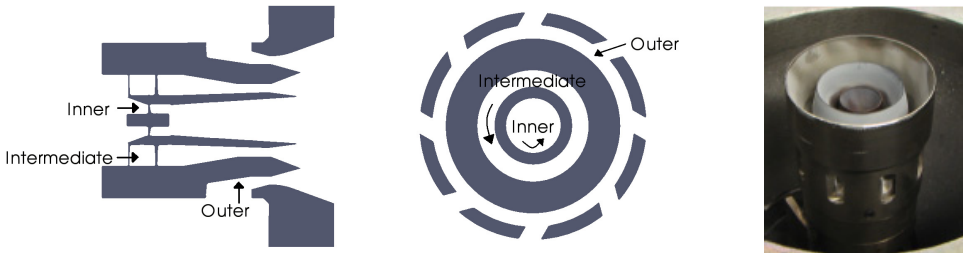

Figure 4.4: *(Left) A diagram showing a longitudinal cross section of the TARS burner. (Middle) A diagram showing a perpendicular cross section of the TARS burner. (Right) A photograph of the TARS burner.*

plenum chamber (361.9 mm long) and is set up vertically. When air flows through the flow conditioning chamber, it passes through a perforated cone and then through a sequence of five fine mesh screens to create a uniform velocity distribution before the air enters the plenum chamber, where the burner is mounted. In the plenum chamber the air is mixed with the fuel if the burner operates under premixed conditions. When premixed conditions exist, the fuel is injected about 230 mm upstream from the base of the TARS burner. A nearly complete mixing of air and fuel is then achieved before the mixture produced enters the TARS burner. If the burner operates under non-premixed conditions the fuel is injected through small holes to the shear layer between the intermediate and the outer swirler. The air mass flow rate is measured by a digital flow meter (Master Touch 8000 MP/NH, with a ± 0.0001 kg/s accuracy), the fuel flow being controlled by a needle valve and a digital flow meter (Siemens SITRANS F C MASS 6000, having ± 0.00001 kg/s accuracy).

The easy exchangeability of different swirler configurations makes the TARS burner very useful for studies of flashback, liftoff and blow-out. Flashback refers to flame propagation upstream into the premixing zone, whereas liftoff refers to conditions resulting in a flame being stabilized at some distance downstream from the burner, its not being attached to the burner. A blow-out occurs when the flame has been lifted so far downstream that it extinguished. The flame here is too lean, due to dilution of the surrounding air. Events of this sort are unwanted in gas turbine combustors, since they can damage both the upstream and the downstream hardware components. It is thus important to understand the mechanism behind such events. Flame dynamics, flame stabilization and flashback were studied with this in mind using simultaneous measurements of flame position, fuel distribution and velocity field. The results of these studies are reported in Papers I-III and are presented in section 5.1.

4.3 Industrial gas turbine burner test facilities

An industrial gas turbine can consist of up to 30 individual burners and, as mentioned earlier in section 4.2, it can be very difficult to study with use of advanced optical tech-

niques. Nevertheless, significant knowledge regarding gas turbine combustion, such as flame position and fuel distribution, can be achieved by studying even a single burner. Studies of different industrial gas turbine burners were performed, both in a high-pressure combustion test rig in Lund and in an atmospheric pressure combustion rig at Siemens Industrial Turbomachinery AB in Finspång. In the high-pressure combustion facility in Lund, fuel vaporization and consequent mixing of the fuel with air were investigated in a gas turbine pilot burner, using an LPP injector in a swirling co-flow. At Siemens in Finspång, several different Dry Low Emission (DLE) burners used in the SGT-800 and the SGT-700 industrial gas turbine were studied through visualizing the flame position and the fuel distribution. Both the high-pressure combustion facility in Lund and the atmospheric pressure combustion rig at Siemens in Finspång are described briefly in the sections that follow. A more detailed description of the atmospheric pressure combustion rig at Siemens can be found in [49].

4.3.1 Lund high-pressure combustion facility

The high-pressure combustion test rig in Lund is an optical test rig designed for studies of gas turbine and aero-engine combustion at elevated pressures under industrial-like conditions. The test facility provides an air flow rate of up to 1.2 kg/s at an inlet temperature of up to 800 K and an inlet pressure of up to 16 bar. Both liquid and gaseous fuels can be used. For liquid fuels, it enables a flow rate of up to 100 kg/h to be achieved and for natural gas the rate attained being up to 86 kg/h.

The air supplied by the compressor is introduced into the outer pressure vessel of the rig, and acts as cooling air for the combustion chamber before it is directed through an electric preheater. After leaving the preheater, the air passes through a mass flow meter and a plenum in which the burner is mounted, prior to its entering the combustion chamber. The combustion chamber has a square cross-section (100 mm $\times$ 100 mm $\times$ 135 mm) and 5 mm thick quartz windows on four sides, perpendicular to the flow path. The optical combustion chamber is housed in a larger high-pressure chamber having 20 mm thick quartz window, which provides optical access to each window of the combustion chamber, see Fig. 4.5. There are two lines of fuel supply to the burner: the pilot and the main fuel-supply lines. The amount of fuel provided is controlled by the fuel mass flow meter and a fuel pressure meter. The combustion products then pass through a 60 mm orifice, which controls both the pressure in the chamber and the pressure drop downstream down to $\sim$1 bar. The product gases are then cooled by water jets before they escape through the exhaust system. Combustion can occur within interchangeable ducts making it possible to study different combustion arrangements such as LPP and RQL. The optical accessibility makes it possible to study liquid fuel vaporization and fuel/air mixing, for example, using optical or laser-based techniques, see Paper IV and [50]. In addition, an afterburner enables studies of fuel evaporation to be carried out, a steam generator for studies of combustion in humid air also being provided.

The combustor duct in the test was an aero-engine LPP injector designed and tested by Rolls-Royce [51]. The duct is short and has relatively short residence times, a high

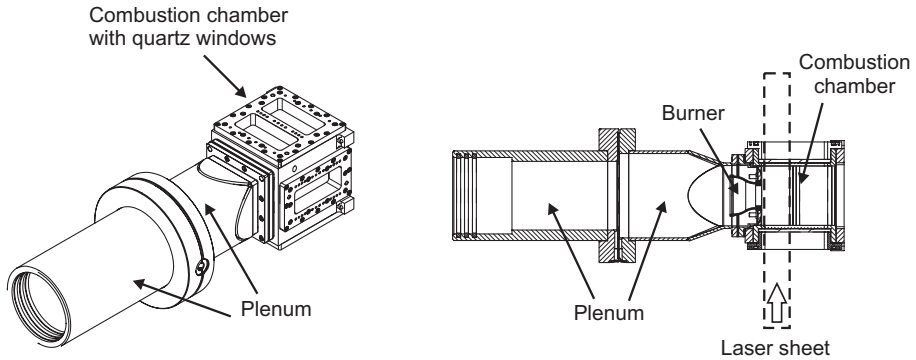

Figure 4.5: *(Left) A 3D drawing of the test-section of the high-pressure combustion test rig. The plenum and the combustion chamber, with its quartz windows, can be seen. (Right) A top view of the test section showing the plenum, burner position, combustion chamber and laser sheet position.*

degree of swirl being induced by a series of axial blades and there being a pilot flame which is stabilized by a V shroud. Only the pilot flame was studied in the tests, its injector being a pressure-swirl atomizer with interchangeable nozzles that can take on different spray cone angles. The results of the tests are reported in Paper IV and are presented in section 5.2.

4.3.2 Siemens atmospheric pressure combustion rig

The atmospheric pressure combustion rig at Siemens in Finspång is an optical test rig designed for studies of industrial gas turbine burners at atmospheric pressure. The layout and a drawing of the main parts of the test rig are shown in Fig. 4.6. The combustion chamber consists of a casing and a liner that is cooled convectively. It has a single-can configuration with a cross section having expansion ratio similar to that of the SGT-800 combustor. The combustion air and the cooling air are separated in order to be able to control the temperature of the liner wall. The cooling air is used to control the liner-wall temperature, its being possible to provide the wall with either a constant or a variable temperature. The combustion air is preheated prior to its entering the plenum, where it is evenly distributed to the burner. It can be preheated up to 820 K. During the measurements, reported in Papers V and VI, the temperature was approximately 690 K. The air flow rate is measured on the basis of the pressure drop from an orifice, with an accuracy of approximately $\pm 1\%$. There are three lines of fuel supply to the burner: the pilot, the main and the central one. These are individually controlled by Coriolis mass flow meters, each of them having a maximum error in the range of 0.1 to 0.8%. The test rig has an air flow rate of up to 600 g/s and a fuel flow rate of up to 20 g/s.

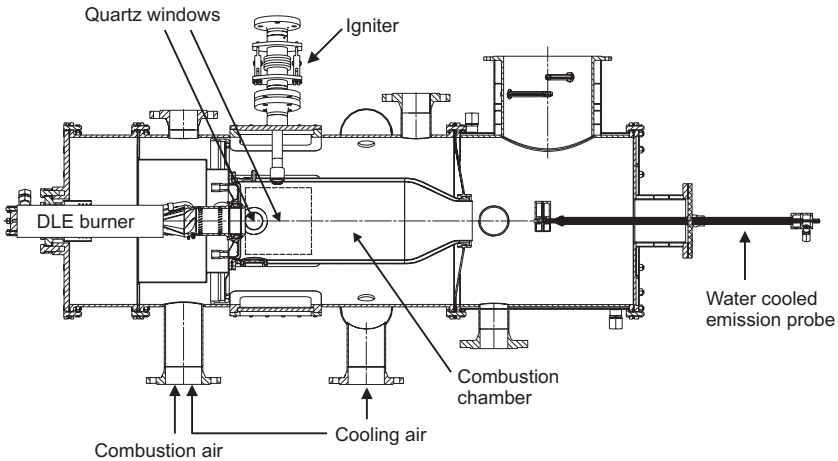

Figure 4.6: *Layout of the atmospheric combustion test rig at Siemens, Finspång.*

Optical access is possible through quartz windows on three sides of the liner, allowing optical and laser diagnostic measurements to be carried out. Originally, the test rig was equipped with circular quartz windows having a diameter of 50 mm (the small circle in Fig. 4.6), but it was upgraded later to having square quartz windows with dimensions of 170 mm $\times$ 200 mm (the dashed square in Fig. 4.6). It is also possible to insert emission probes, pressure sensors and thermocouples for monitoring and measuring emissions, the dynamic pressure and temperatures at different positions in the combustion chamber. Visualization of the flame position and fuel distribution of different DLE burners and of operating conditions by means of OH and acetone PLIF was performed, the results being presented in section 5.3 and in Papers V and VI.

The main part of a DLE burner used in the measurements is shown in Fig. 4.7. The flow enters the swirl generator in a combined tangential/axial/radial direction, the radial component causing a high axial velocity at the centerline, the main fuel being injected into the air stream through nozzles in the swirl generator. The burner itself consist of four quarter-cones, which are shifted with respect to each other so as to create a swirling flow. They are connected to a circular mixing tube with a secondary air inlet by means of film air rows, as can be seen in Fig. 4.7. The swirling air/fuel mixture passes through the mixing tube and enters the combustion chamber, where it expands in a radial direction, due to the imposed swirl. Around the edges of this radially expanding swirling air/fuel jet, the air and the fuel are mixed to produce a combustible mixture that ignites due to the high temperature. The flame takes the form of a short wrenched tube that fold back on itself around the central recirculation zone in the middle of the combustion chamber. In addition, there are 12 pilots equally distributed circumferentially around the burner nozzle, one of these being inactive during the measurements.

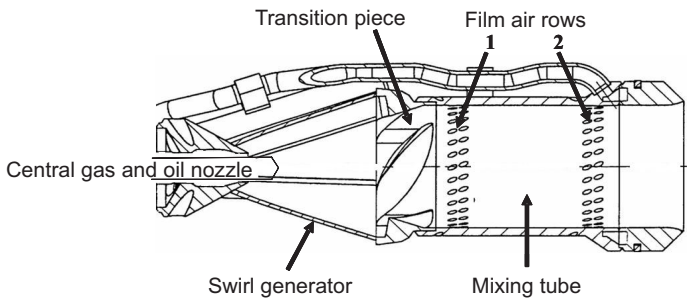

Figure 4.7: *The main parts of the DLE burner used in the measurements.*

4.4 High-pressure vessel and burner

In a gas turbine, the combustion of liquid or gaseous fuels occurs under high pressure (of up to approximately 30 bar). It is thus important to have knowledge of how the fuels behave at high pressure levels. To be able to study different fuels under high pressure, a High-Pressure Vessel and Burner (HPVB) were used in a study in collaboration with Eindhoven University of Technology, where the HPVB was also designed and constructed [52]. The HPVB allows studies of different flame types (premixed, partially premixed and diffusion) involving both liquid and gaseous fuels at pressures of up to 30 bar. A diagram of the HPVB is shown in Fig. 4.8. The design of the burner is based on a burner used by Smooke et al. [53, 54]. It is a coflow burner with a fuel tube (having an inner diameter of 4 mm) surrounded by a coflow (having an inner diameter of 50 mm). The nozzle of the burner is tapered to reduce recirculation from the burner tip and to improve the stability of the fluid-ambient interface. The burner design is adapted, in comparison with the burner used by Smooke et al., so as to fit into the high-pressure vessel and to work at pressures of up to 30 bar. The fuel and the carrier gas are mixed and controlled in an evaporation system termed CEM (Controlled Evaporator Mixer) that provides a stable fuel vapor stream at temperatures of up to 473 K. In order to avoid condensation of the fuel vapor, both the tube that connects the CEM to the burner and the burner itself are heated. All the gases and the gaseous fuel flows are controlled by mass flow controllers (Bronkhorst, EL-FLOW) having a $\pm$ 5% uncertainty, the liquid fuel flow being controlled by a liquid flow meter and by the CEM. The HPVB provides optical access for optical and laser diagnostic measurements through four quarts windows (each having a diameter of 50 mm), allowing assessment and development of techniques to be carried out at elevated pressures. In addition, there are eight connectors into which measurement equipment such as thermocouples and pressure sensor can be inserted. Comparisons between experimental results and modeled data are presented in Paper VII and in section 5.4.

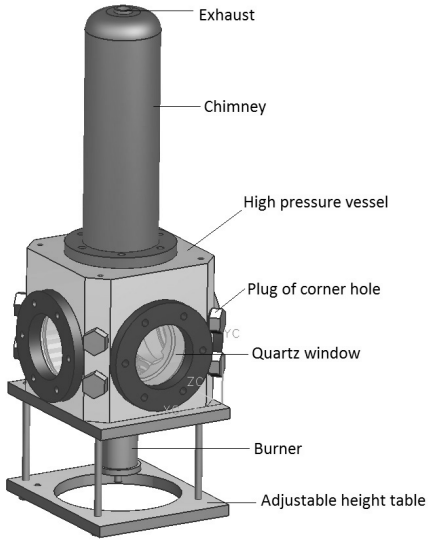

Figure 4.8: *The high-pressure vessel and its assembled parts.*

Chapter 5

Applications and results

This chapter summarizes the experimental work conducted within the framework of the thesis. The measurements and results presented are selected mainly from the papers included in the thesis, but some unpublished work by the author is also included. The chapter is divided into four sections. In the first section, 5.1, the measurements for characterization of the TARS burner are discussed. Section 5.2 concerns the high-speed fuel/OH imaging of a gas turbine pilot burner in the Lund high-pressure combustion facility, section 5.3, in turn, deals with the OH/fuel visualization measurements performed on different industrial gas turbine burners on-site at Siemens in Finspång. In the last section, 5.4, the measurements in the high-pressure vessel and burner (HPVB) are discussed.

5.1 Characterization of the TARS burner

The TARS burner, described in section 4.2, allows studies of turbulent flames under a wide range of operating conditions (e.g. equivalence ratio, air and fuel mass flow, Reynolds number and swirler configuration) to be carried out. The burner had previously been studied experimentally by use of such techniques as PIV, laser Doppler velocimetry (LDV) and OH chemiluminescence imaging, and numerically, by use of LES, in both non-reacting and reacting flows [55–57]. In the present work, flame and flow dynamics were studied by means of the simultaneous visualization of flame position (OH PLIF), fuel distribution (acetone PLIF) and flow field (PIV). The results are presented in Papers I-III and a summary is given in sections 5.1.1 and 5.1.2.

Important features of the flow could be extracted from the measured data sets by use of the data evaluation method Proper Orthogonal Decomposition (POD). POD is an established statistical tool within fluid mechanics [58] and is widely used to analyze non-reacting flows, and has also been used recently in combustion applications to highlight flame and flow dynamics [59, 60]. The results of a POD analysis are a set of orthogonal eigenmodes representing coherent flow and flame structures ordered in terms of their contribution to the total energy involved. In the present work, POD was applied to

the results so as to reveal relationships between the flame and the flow, the results being reported in Papers I-III.

5.1.1 Effect of different swirler designs on flame and flow dynamics

Paper I reports on studies of how different swirler designs affected the flame and the flow dynamics. The flexibility of the TARS burner makes it possible to study different swirler configurations, in the present study three different configurations being employed. The vane angles and the rotation of the different swirlers in the three configurations are summarized in Table 5.1.

Table 5.1: *Vane angles and rotations of the three swirlers in the different configurations.*

	Swirler	Vane angles	Rotation
Case A:	inner	-	-
	intermediate	50°	clockwise
	outer	50°	clockwise
Case B:	inner	50°	clockwise
	intermediate	50°	clockwise
	outer	50°	clockwise
Case C:	inner	25°	counter-clockwise
	intermediate	25°	clockwise
	outer	25°	clockwise

The burner was operated in a premixed mode, and methane being injected approximately 230 mm upstream from the burner nozzle. Simultaneous measurements of OH PLIF, acetone PLIF and PIV were used to visualize the flame position, fuel distribution and flow field, respectively. A schematic presentation of the experimental setup is shown in Fig. 5.1. A frequency-doubled dye laser operating with use of Rhodamine 590 dye was employed for exciting the OH radicals and the acetone molecules simultaneously with use of the same laser pulse. The dye laser was pumped by the second harmonic, i.e. 532 nm, of an Nd:YAG laser. The OH and acetone PLIF signals were detected simultaneously by means of an ICCD camera equipped with a Nikkor UV-lens (f=105 mm, f/4.5). A stereoscope was used to store the two signals in two separate parts of the ICCD sensor. To eliminate scattering brought about by the laser light and prevent interference between the OH and acetone PLIF signals from occurring, a combination of filters (a UG11 (Schott) filter and a high-reflection filter (HR 275-295 nm)) was used for the OH signal and another combination of filters (a WG335 (Schott) filter and a shortpass 500 nm filter) for the acetone signal. The laser beam was formed into a 50 mm wide laser sheet by use of sheet-forming optics. Two different orientations of the laser sheet were employed, one of them vertical and the other tilted (20 degrees with respect to the horizontal plane): see the cut-in section in Fig. 5.1. The tilted angle was necessary to enable positioning of a UV-enhanced aluminium mirror for reflecting of the PLIF signal to the ICCD camera to take place. The OH and the acetone PLIF measurements

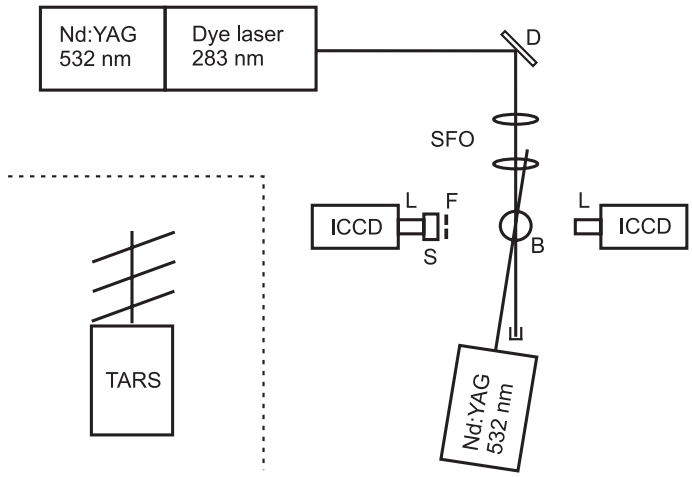

Figure 5.1: *Experimental setup used for the simultaneous PIV, OH- and acetone PLIF measurements in the TARS burner. The abbreviations denote the following: D, dichroic mirror; SFO, sheet-forming optics; B, TARS burner; L, camera lens; S, stereoscope; F, filter; ICCD, intensified CCD camera. The cut-in section shows the different laser sheet positions above the TARS burner. Only results from the vertical and the lowest of the tilted laser sheets are reported in Paper I.*

were performed almost simultaneously with velocity measurements involving PIV, and with use of overlapping laser sheets. A double-pulsed Nd:YAG laser was employed here and the first PIV laser pulse being fired 12 μs after the PLIF pulse in order to eliminate any interference from the PLIF laser system. The time separation between the two PIV pulses was 20-30 μs, depending on the experimental conditions. The laser sheet was approximately 1-2 mm thick and TiO_2 particles were used for seeding. The seeding particles were injected continuously approximately 230 mm upstream from the burner nozzle so as to obtain a homogeneous distribution.

Average OH PLIF and acetone PLIF signal distributions for the three different swirler configurations are shown in Fig. 5.2. The inflow conditions are the same for each of the three configurations. The top section (above y/D=0.7) of the acetone field is blanked due to excessive noise that originated from interference produced by the OH PLIF signal. There is a difference between having no swirler in the center, as in case A, and having a swirler in the center, as in case B and case C. In case A, in which there was no swirler in the center, unburnt fuel was found in the center part (x/D=$\pm$0.2). The low-swirl case (C) and the high-swirl case (B) are alike in the qualitative features they show, displaying no signal from unburnt fuel in the center part, the fuel signal being located close to the inner shear layer. The apparent difference between case B and case C is that the unburnt fuel penetrates further downstream in the shear layer in case C (y/D=0.6) than in case B (y/D=0.4). Both case B and case C involve a higher

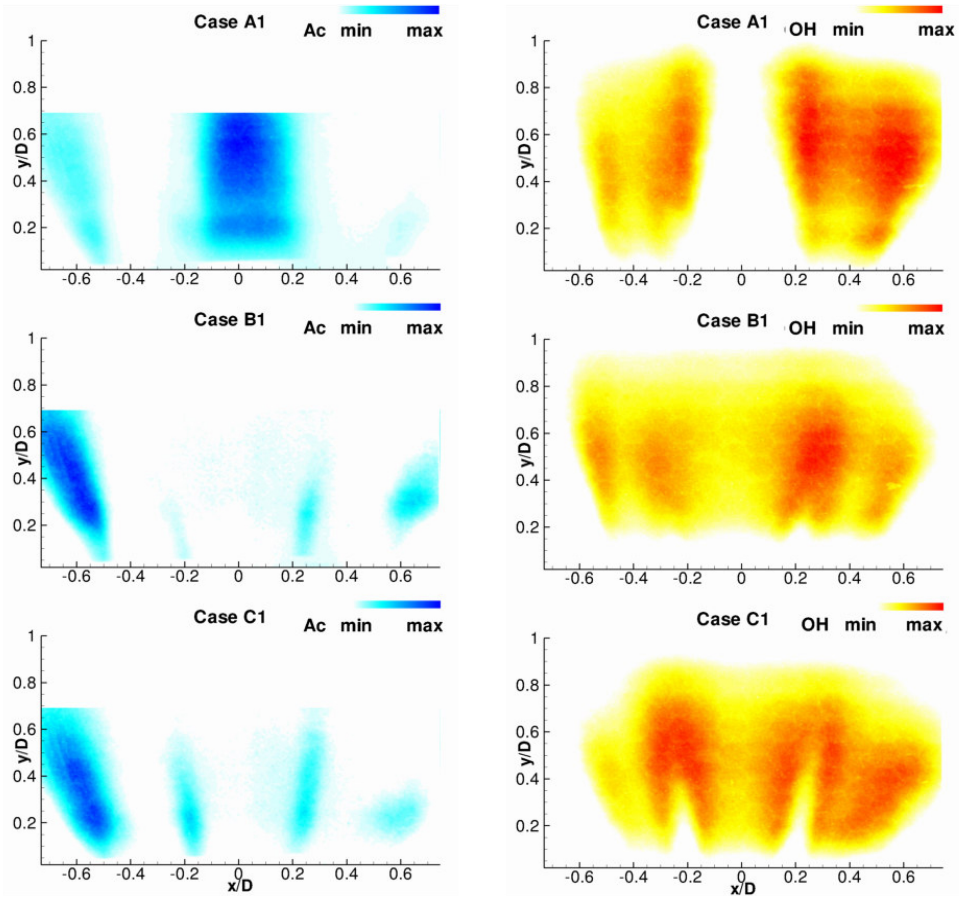

Figure 5.2: *Average fuel distribution (left columns) and OH distribution (right columns) for configuration A1 (no inner swirler), B1 (high level of swirl) and C1 (low level of swirl). The axes are normalized with the burner outlet diameter D=50.8 mm.*

level of swirl than case A. This results in greater shear in the azimuthal direction and to an increased tendency to form recirculation zones. Since these effects help to improve the fuel/air mixing, no unburnt fuel is found in the central part in either case B or case C. The two outer swirlers induce, for each of the three configurations an annular swirling jet having inner and outer shear layers, by means of which the flame front is stabilized. No significant differences are to be noted in the outer part since the outer swirler configuration is the same in all three cases. The corresponding velocity fields for the three configurations show certain differences, see Paper I, indicating that differences in swirler configuration affect both the flame and the flow dynamics.

Single-shot images of OH PLIF and acetone PLIF signal distributions for case B in the lowest of the tilted laser sheet positions are shown in Fig. 5.3. Close agreement between the OH and the acetone PLIF signal distributions were found, the structures being captured in fine detail. Two annular swirling jets were identified, with no PLIF signal from unburned fuel being found in the center part. This indicates the fuel/air mixing functions well, even though the measurement region is positioned close to the burner surface. Further information regarding the experiments and the results obtained can be found in Paper I.

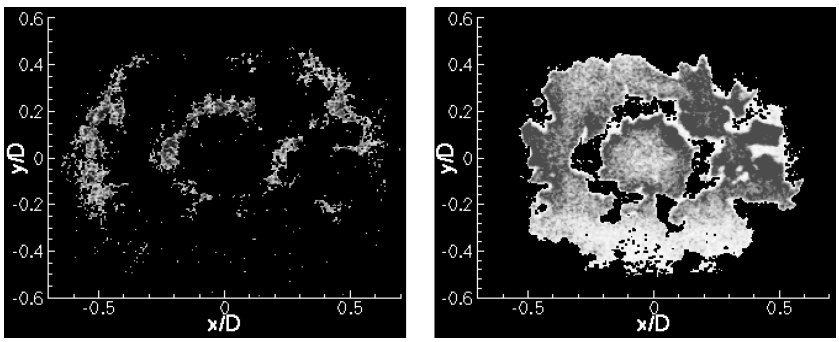

Figure 5.3: *Single-shot images of the acetone PLIF signal distribution (left) and the OH PLIF signal distribution (right) for case B in the lowest of the tilted laser sheet positions. The axes are normalized with the burner outlet diameter D=50.8 mm.*

The results for the tilted laser positions were analyzed further to extract information about structures in the azimuthal direction. The axes were transformed into polar coordinates: (x/D,y/D)→(r/D,θ) and the image intensity was binarized. The analysis was focused on PLIF signal profiles at different radii. It was found that the position of the unburnt fuel was in the range of r/D=0.22-0.24 with a width of r/D=0.08-0.09, see Paper II. The change in the flow rate and in the equivalence ratio did not affect the position of the fuel PLIF signal distribution relevantly, indicating the position of the annular jets to be determined by the swirler geometry. To estimate the modes in the azimuthal direction, an algorithm to count the number of unburnt fuel pockets along r/D=0.23 was implemented. Analysis of the results indicated the modes to be in the range of n=4-10, see Paper II. The appearance of the lower modes can be due to the fact that, even in the region just above the outlet of the burner, the highly turbulent field which is generated inside the TARS favors the merging of the fuel jets. The higher modes can be considered to be due to small-scale wrinkling of the unburnt fuel pockets. Further information regarding the analysis can be found in Paper II.

5.1.2 Flashback and flame dynamics studies

The objective of the work reported in Paper III was to study flashback and flame dynamics under different operating conditions of the TARS burner. Flashback is an unwanted event in gas turbine combustors since it can overheat and damage upstream hardware components and increase pollutant emissions, through flame propagation upstream into the premixing zone. Since the problem becomes more severe as the pressure and the air and flame temperatures increases, it is important to know under what operating conditions flashback occurs. Simultaneous visualization of the flame position (OH PLIF) and the flow field (PIV) of the TARS burner were employed for studying flame dynamics and flashback.

While the measurements were being obtained, all three swirlers were co-rotating at 50 degree vane angles. A mixing tube having the same inner diameter, D=50.8 mm, as the burner nozzle was placed above the burner nozzle in order to study the air/fuel mixing process. The tube, which had a length of one diameter D, was made of stainless steel. The burner was operated under non-premixed conditions, the methane being injected through small holes into the shear layer between the intermediate and the outer swirler. Figure 5.4 shows a schematic view of the experimental setup. The OH radicals, used as reaction zone markers, were excited by the $Q_1(8)$ transition at around 283 nm, using a frequency-doubled dye laser making use of Rhodamine 590 dye. The OH PLIF signal was detected using an ICCD camera equipped with a Nikkor UV-lens (f=105 mm, f/4.5). The combination of a UG11 (Schott) filter and a high-reflection filter (HR 275-295 nm) was used to reduce the scattering light originating from the laser

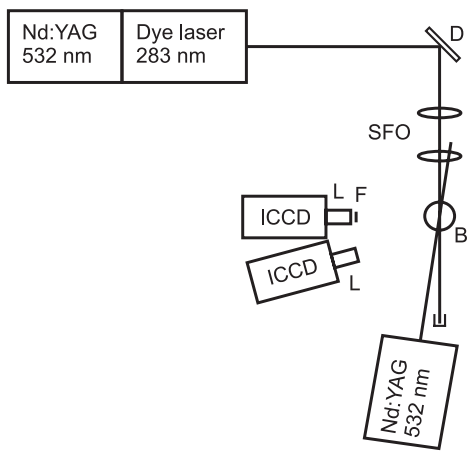

Figure 5.4: *The experimental setup used for simultaneous PIV/OH PLIF measurements in studies of flashback and flame dynamics studies in the TARS burner. The abbreviations denote the following: D, dichroic mirror; SFO, sheet-forming optics; B, TARS burner; L, camera lens; F, filter; ICCD, intensified CCD camera.*

pulse. A 50 mm high vertical laser sheet was formed by use of sheet-forming optics. The OH PLIF measurements were performed almost simultaneously with the velocity measurements, making use of PIV. A double-pulsed Nd:YAG laser was used here, the first PIV laser pulse being fired directly after the PLIF laser pulse. The time separation between the two PIV laser pulses was 50 µs. The laser sheet was approximately 1-2 mm thick and TiO_2 particles were used for seeding and the seeding particles were injected continuously approximately 230 mm upstream from the burner nozzle so as to obtain a homogeneous seeding distribution.

To examine flame stabilization and flashback, probability density functions (PDF) of the axial velocity for different equivalence ratios were calculated at a position along the symmetry axis half a diameter above the premixing tube. The results are shown in Fig. 5.5, in which four different states can be observed. The first state involves conditions close to lean blow-out, ϕ=0.66. The PDF shows a peak at a normalized axial velocity of around zero, the flame being stabilized above the premixing outlet. An example of a single-shot image of the OH PLIF signal distribution for this equivalence ratio is shown in Fig. 5.6a. The second state can be observed at ϕ=0.68 and ϕ=0.71. There, the stagnation point of the flame fluctuates in the axial direction around the outlet of the premixing tube. Sometimes the stagnation point is positioned inside the premixing tube. The third state, at ϕ=0.72 and ϕ=0.75, is an unstable state involving bimodal behavior. The flame moves from a stagnation point inside the premixing tube to a stagnation point outside of it. Determining at what equivalence ratios this occurs is extremely important, since the flame here is close to flashback. In the fourth state, at ϕ=0.76, the stagnation point is always inside the premixing tube and the flame is positioned there, indicating flashback to have occurred. Figure 5.6b provides an example

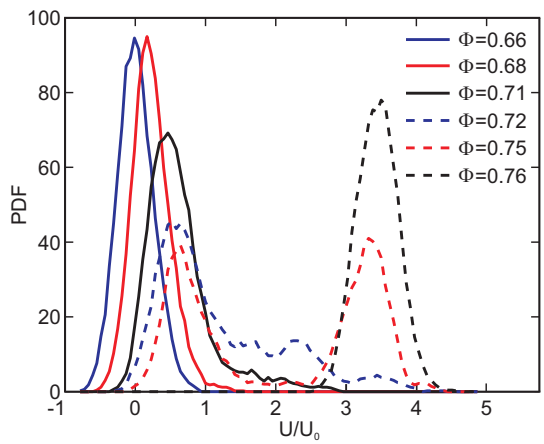

Figure 5.5: *The probability density function (PDF) of the axial velocity at a position half a diameter above the premixing tube along the symmetry axis, shown for different equivalence ratios. Adapted from Paper III.*

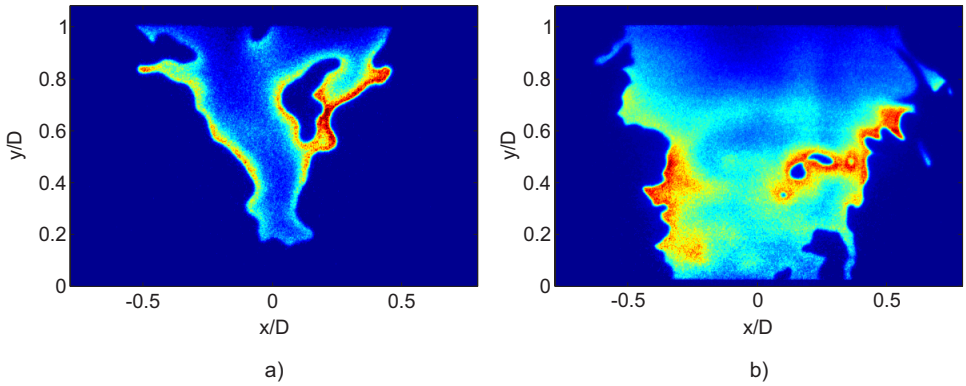

Figure 5.6: *A single-shot image of the OH PLIF signal distribution for (a) ϕ=0.66 and (b) ϕ=0.76. The axes are normalized with the burner outlet diameter D=50.8 mm.*

of a single-shot image of the OH PLIF signal distribution at this equivalence ratio. The flame looks, in terms of its shape, like a jet having a flame width equal to the diameter D of the premixing tube. These observations indicate the flame to be more sensitive to flashback in the case of an increase in the equivalence ratio, a matter that can be explained by the increase in the laminar flame speed that occurs. Further information regarding the experiments and the results can be found in Paper III.

5.2 High-speed fuel/OH imaging in a gas turbine pilot burner

Understanding fuel vaporization and its consequent mixing with air in the combustion chamber is important in order to achieve optimal combustion in gas turbine applications. Fuel visualization is a powerful tool for such studies, since it yields information about the fuel distribution. In Paper IV, different laser techniques were applied to a gas turbine pilot burner in order to visualize flame position and fuel distribution. Laser-induced fluorescence was chosen for visualizing the flame position and the liquid and vaporized fuel distribution, whereas the Mie scattering technique was chosen for visualizing the liquid fuel distribution.

The measurements were performed in the Lund high-pressure combustion facility described in section 4.3.1. The combustor duct used in the tests was an aero-engine LPP injector with an integrated pilot burner. The injector was a pressure-swirl atomizer fuel injector surrounded by coflow generated by outer swirl vanes and perforations in the heat shield. Two fuels, Jet A and biojet, were studied using the pilot flame of the burner. Biojet has certain advantages under operating conditions found, in which Jet A limits the use of optical diagnostics due to its high absorption characteristics in the UV region and to the heavy soot formation occurring under some operating conditions [50, 61]. Three different air-to-fuel ratios were tested for each fuel, all tests being run under lean conditions at T_{30}=563 K and p_{30}=3 bar (abs).

The high-speed laser and the camera system, described in section 3.3, were used during the tests, Fig. 5.7 provides a schematic view of the experimental setup. The second and fourth harmonic from the Multi-YAG laser cluster, at 532 nm and 266 nm, were used for Mie scattering and fuel PLIF, respectively. To generate the proper wavelength for OH PLIF (283 nm), an OPO laser (premiScan/MB, GWU) was used, which was pumped by the third harmonic, at 355 nm, from the Multi-YAG laser cluster. The PLIF signals generated were detected by a high-speed framing camera equipped with a B. Halle UV-lens (f=100 mm, f/2), different filter combinations being employed depending on the measurement techniques involved. The signals were directed at the camera via a UV-enhanced aluminium mirror, through a window mounted on top of the combustion chamber, the region detected being 40 × 75 mm in size.

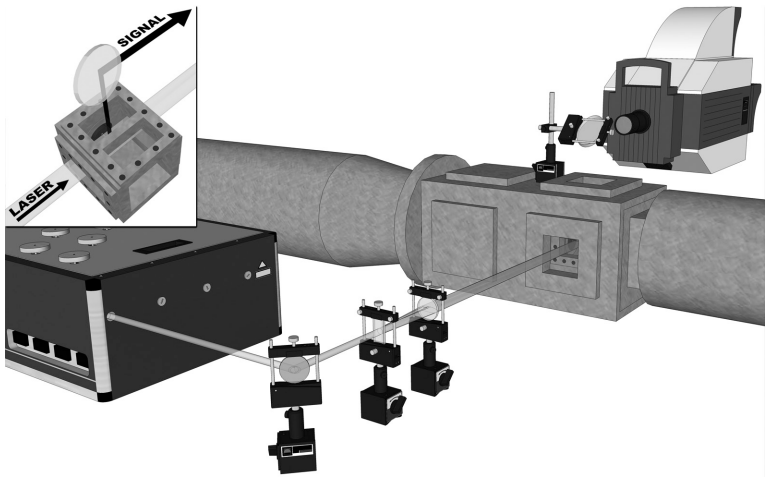

Figure 5.7: *The experimental setup showing, the Multi-YAG laser, the high-pressure rig, the optics and the camera employed. The cut-in section shows the optical combustion chamber.*

Figure 5.8 presents image sequences of seven frames each, showing the fuel PLIF signal distribution of Jet A (Fig. 5.8a) and of the biojet (Fig. 5.8b) at p=3.0 bar (abs), a time separation of 145 μs between consecutive images being employed. The V-shape of the fuel spray can be observed and larger structures can be identified, its being possible to follow them as the injected fuel vaporizes. The PLIF signals show both vaporized and liquid fuel. The Mie scattering technique was employed in order to obtain an indication of where the fuel is still in the liquid phase. Mie scattering is elastic scattering of radiation from particles and droplets, its detection being a suitable indicator of the liquid phase of the fuel. An image sequence of seven frames showing the Mie scattering of the biojet is shown in Fig. 5.8c. As can be observed, it takes a certain distance downstream for the fuel to be completely vaporized. One should note, however, that the fuel PLIF and Mie scattering measurements were not performed simultaneously, as would have been the ideal procedure.

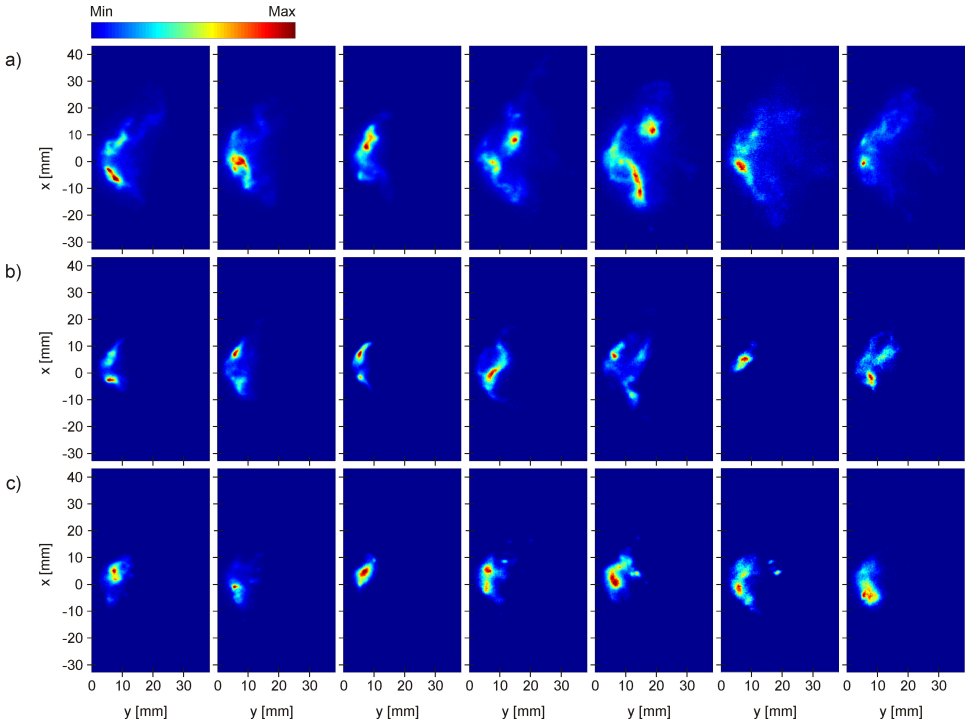

Figure 5.8: *Image sequences of fuel PLIF and Mie scattering at p=3.0 bar (abs). (a) fuel PLIF of Jet A at an air-to-fuel ratio of 82. (b) fuel PLIF of biojet at an air-to-fuel ratio of 83. (c) Mie scattering of biojet at an air-to-fuel ratio of 83. The image sequences are from left to right, the time separation between consecutive images being 145 µs.*

For the investigation of flame position it was necessary to perform measurements with the laser tuned both on and off an OH transition, since the biojet itself can be excited in the same wavelength region as OH can. With use of this procedure, it is possible then to distinguish spatially between contributions from OH PLIF and from fuel PLIF. The procedure is not performed simultaneously for the two. Figure 5.9a shows a single-shot image of an OH distribution for the biojet, the laser being tuned to an OH transition, Fig. 5.9b presenting an example of another single-shot image in which the laser is tuned off an OH transition. In comparing these images, one can conclude that OH PLIF signals appear both inside and outside of the fuel spray. Figure 5.9c presents an image sequence of three frames showing the OH PLIF signal distribution of the biojet. Comparing the image sequence with the off OH transition image, Fig. 5.9b, enables one to identify the expected positions of the flame and the burnt gas regions.

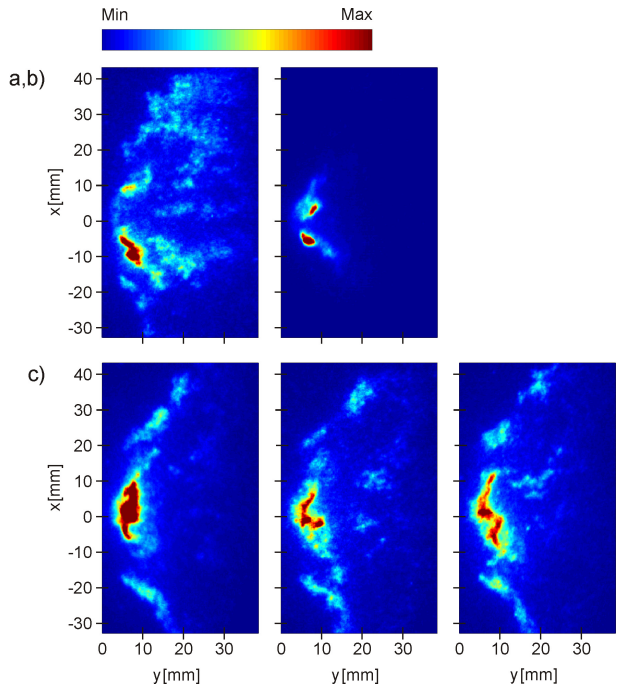

Figure 5.9: *OH PLIF signal distribution images of biojet at an air-to-fuel ratio of 76 and p=3.0 bar (abs). (a) A single-shot image in which the laser is tuned to an OH transition. (b) A single-shot image in which the laser is tuned off an OH transition. (c) Image sequence of an OH PLIF signal distribution with the laser tuned to an OH transition and with a time separation of 145 µs between consecutive images.*

In addition to high-speed imaging, the laser absorption effects for Jet A with use of 266 nm excitation, that had been an issue in previous studies [50, 61], was investigated. Measurements performed in a heated cell indicated that the absorption effect could be avoided by using longer excitation wavelengths, see Paper IV. Therefore, both 266 nm and 300 nm were used as excitation wavelengths in the fuel PLIF measurements, the average fuel PLIF images there indicating the problem of laser absorption to be decreased by use of longer excitation wavelengths. Under the relative lean conditions here, however, the effect was found to be only minor.

5.3 PLIF experiments in industrial gas turbine burners

Laser diagnostics were applied to several industrial gas turbine burners of the type used in SGT-700 [62] and SGT-800 [48] to study their combustion characteristics. This was done in collaboration with Siemens Industrial Turbomachinery AB, the work be-

ing performed on-site at Siemens in Finspång in the atmospheric pressure combustion rig described in section 4.3.2. To visualize the flame position and fuel distribution in different natural gas fueled industrial gas turbine burners and under different operating conditions (involving equivalence ratio, flame temperature and mass flow rate, for example), measurements of laser-induced fluorescence were performed. Four different measurement campaigns were carried out in the course of this work, their being discussed in chronological order in sections 5.3.1-5.3.4.

Investigating flame position, the OH radical was chosen as a flame front marker since it is formed in high concentrations in the high-temperature regions close to the flame front. The OH radical is also a marker for post-flame regions due to its long lifetime during the combustion process. Since natural gas (methane) does not fluoresce when illuminated with UV radiation, a fluorescent tracer added to the fuel was needed. Acetone was chosen here as the fuel tracer since it allows relatively low seeding levels to be employed and since it has a strong fluorescence signal and high vapor pressure. The OH PLIF measurements were performed using a combined Nd:YAG/dye laser system tuned to laser radiation at 283 nm, which is a proper wavelength for OH excitation. Since, as previously discussed in section 2.1.3, acetone has a broad absorption spectrum and can thus be excited with the same wavelength as used for OH PLIF, the same laser system was used to carry out both the OH PLIF measurements and the acetone PLIF measurements, simultaneously. The laser beam was formed into a laser sheet and directed into the combustion chamber either through one of the side windows (Fig. 5.10a) or through the bottom window (Fig. 5.10b), depending on the experimental configuration. The fluorescence signals generated are then detected using ICCD cameras equipped with appropriate Nikkor lenses and filters. For the case in which the laser sheet is directed through one of the side windows, a UV-enhanced aluminium mirror is used to guide the PLIF signals to the cameras. A UV-Nikkor lens (f=105 mm, f/4.5) and a combination of a UG11 (Schott) filter and a high-reflection filter (HR 275-295 nm) were used to collect the OH signal, whereas a Nikkor lens (f=105 mm, f/2.5) and a combination of a WG320 (Schott) filter and a shortpass 500 nm filter were used to collect the acetone signal. To separate the OH and the acetone PLIF signals to the respective detectors, a 308 nm optimized high-reflectivity mirror was employed.

A heated seeder built and operated by Siemens was used for seeding the acetone into the natural gas flow. This was achieved by letting the natural gas pass through the acetone seeder before entering the burner. To improve the seeding efficiency, the liquid acetone was preheated to about 45 °C by the seeder being placed in heated water. The heating procedure was necessary in order for sufficient amounts of acetone to evaporate so that the PLIF signal was strong enough to collect. A bypass link was employed so as enable the seeder to be disconnected when a change was made in the operating conditions of the burner. This seeding procedure used in the first two measurement campaigns was controlled manually, the amount of acetone being increased until the PLIF signal was considered to be sufficiently strong. In the third measurement campaign, the seeding procedure was improved by injecting liquid acetone into the fuel, the amount of acetone being regulated by a mass flow controller. The liquid acetone was preheated electrically before it entered a mixing container, where it was mixed with

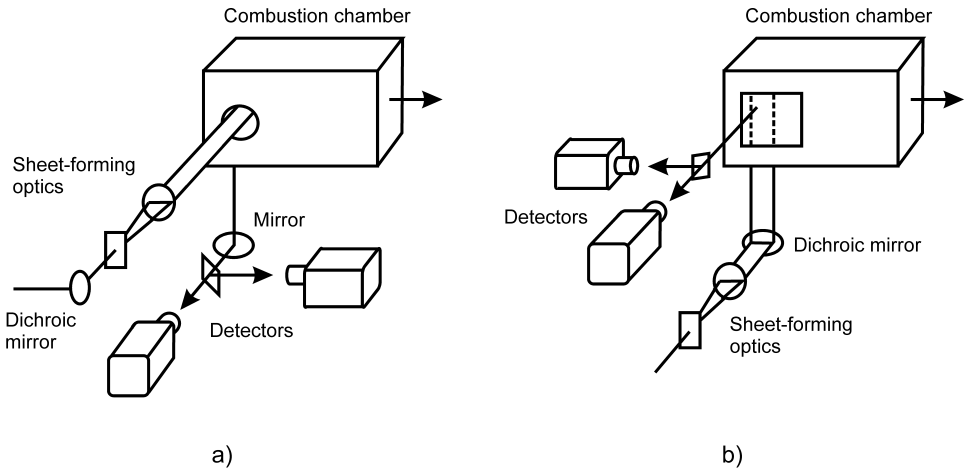

Figure 5.10: *Examples of experimental setups used for OH and acetone PLIF measurements in the gas turbine test rig at Siemens. (a) The laser sheet is directed into the combustion chamber through the side window and the PLIF signal is detected through the bottom window via a UV-enhanced aluminium mirror. (b) The laser sheet is directed into the combustion chamber through the bottom window and the PLIF signal is detected through the side window.*

natural gas, the gas mixture being led from there to the burner. In conducting each of the measurements, approximately 10 vol% of the natural gas was replaced by acetone.

5.3.1 OH and fuel visualization in a gas turbine burner

In the first measurement campaign the objective was to visualize the flame position and fuel distribution in several industrial gas turbine burners through use of OH PLIF and acetone PLIF, carrying this out under a variety of operating conditions. The laser sheet was directed into the combustion chamber through one of the side windows (circular and 50 mm in diameter). The PLIF signal generated was detected by use of the ICCD camera, through the bottom window (likewise circular and 50 mm in diameter) of the combustion chamber via a UV-enhanced aluminium mirror. Examples of single-shot images of OH PLIF and the acetone PLIF signal distribution are shown in Fig. 5.11. The exit of the burner is marked by the dashed line at the left in both images, the flow being from left to right and the laser sheet propagating from bottom to top in the images. The data is scaled between zero and the maximum intensity in the respective images, the contours of the PLIF signals being plotted in the same figure. It can be observed in the OH PLIF image that the burnt regions are located primarily along the centerline downstream from the burner. The single-shot images also indicates the level of turbulent combustion being high, since the flame front, i.e. the contour of the OH PLIF signal, being wrinkled. The acetone PLIF data showed the regions containing

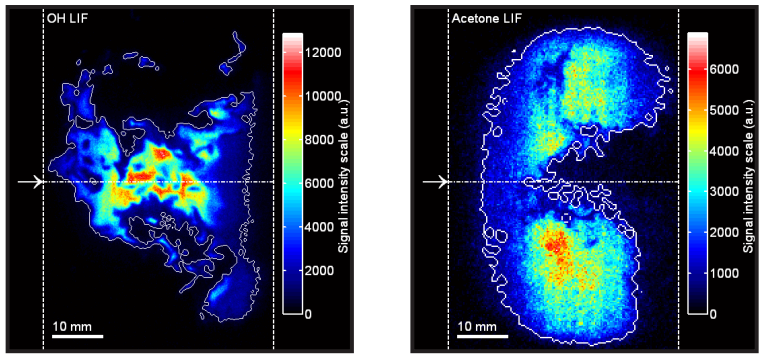

Figure 5.11: *Single-shot images of an OH PLIF signal distribution (left) and an acetone PLIF signal distribution (right) in an industrial gas turbine burner. Note that the images were not recorded simultaneously.*

unburned fuel, i.e. upper and lower parts of the images, to be concentrated to regions around the flame. This indicates regions containing unburnt fuel to be separated spatially from regions in which combustion had occurred, a finding verified in measurements performed simultaneously in the later measurement campaigns. One should note that the OH and acetone images were not recorded simultaneously, which would have been a better procedure. However, simultaneous measurements were performed in later measurement campaigns.

5.3.2 Simultaneous OH and fuel visualization in a gas turbine burner I

As concluded after the first measurement campaign had been completed, OH PLIF and acetone PLIF measurements should preferably be performed simultaneously, this being the procedure in this the second measurement campaign. The experimental set-up in this measurement campaign is similar to that shown in Fig. 5.10a. Two single-shot images of the simultaneous OH PLIF and acetone PLIF signal distribution are shown in Fig. 5.12. The laser sheet propagation in both cases is from bottom to top, the width of the laser sheet being approximately 50 mm and the flow being from the left to the right. The OH intensity is represented by a color scale ranging from black through red to white, the acetone being represented by a color scale ranging from black through green to white. Both the OH and the acetone PLIF intensities are scaled, from zero to 85 % of the maximum intensity in the respective images for easy imaging purposes. As can be seen, the PLIF signals from OH and from acetone match each other very closely. One can also note that the flame front, i.e. the interface between the OH and acetone fields, is wrinkled. In addition, the flame showed strong fluctuations in the axial direction repeatedly, along with fluctuations due to turbulence on a small to intermediate scale.

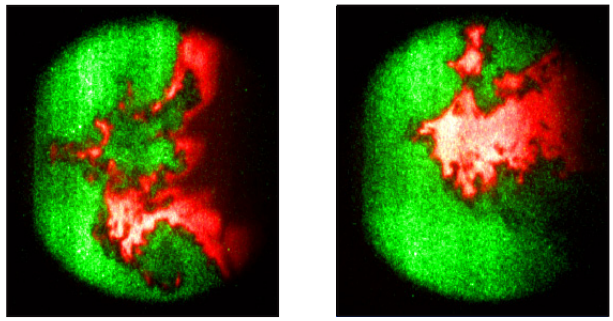

Figure 5.12: *Single-shot images of OH PLIF signal distribution (red) and acetone PLIF signal distribution (green) using simultaneous OH PLIF and acetone PLIF measurements in an industrial gas turbine burner.*

The experimental results were used to validate three different LES models developed jointly by Siemens and the Swedish Defense Research Agency (FOI). Validation of the models was done by comparing the acetone radial PLIF signal profiles with LES profiles at different axial locations (10, 20, 30 and 40 mm downstream from the burner). The comparisons showed the result to agree closely with one of the LES models, see Paper V. Only the center part of the flame was covered in the measurements, however, due to the window being relatively small. To obtain more thorough information on the flame dynamics involved and for better validation of the LES models, the optical access needed to be improved so that the flame in its entirely could be studied, an improvement that was made in connection with the third measurement campaign. Further information concerning the LES models and comparisons of the experimental with the modeled data can be found in Paper V.

5.3.3 Simultaneous OH and fuel visualization in a gas turbine burner II

Since only the center part of the flame had been studied in the two earlier measurement campaigns, the optical access was improved prior the third, large square quartz windows with dimensions of 170 $\times$ 200 mm being installed. This made most of the flame visible and thus made it possible to investigate how the flame behavior was affected by use of operating conditions differing in the Main fuel to total Fuel Ratio (MFR), the Pilot fuel to total Fuel Ratio (PFR) and the Central fuel to total Fuel Ratio (CFR). This had not been possible to study by use of PLIF in the earlier measurements campaigns due to the limited optical access there, which resulted in only a small part of the flame being visible. The PFR and CFR determines the relative amounts of fuel passing through the pilot fuel line and the central fuel line, respectively, and improves the combustion stability within a certain load range. In the burners investigated there were 12 pilots distributed equally in circumferential terms around the burner nozzle, a low PFR value affecting the outer recirculation zones substantially, as can be seen in Fig. 5.13.

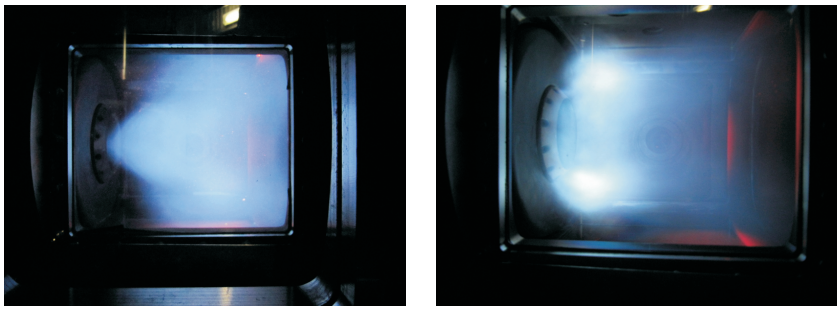

Figure 5.13: *Examples of two typical flame conditions in the combustion rig: Only the main flame is active (left). Both the main and the pilot are flame active (right).*

During these measurements, the laser sheet was directed into the combustion chamber through the bottom window, the PLIF signals being detected through one of the side windows using the same dual detection system as in the second measurement campaign, see Fig. 5.10b. Typical single-shot images of the simultaneous OH PLIF and acetone PLIF signal distribution are shown in Fig. 5.14 for different MFR, PFR and CFR settings. The laser sheet propagation is from bottom to top in the images, the width of the laser sheet being approximately 40 mm. The flow is directed from the left to the right. The OH PLIF signal intensity is represented by a color scale ranging from black through red to white, the acetone PLIF signal being represented by a color scale ranging from black through green to white. Both the OH and the acetone PLIF signal intensities are scaled individually in the respective images from zero to 85 % of

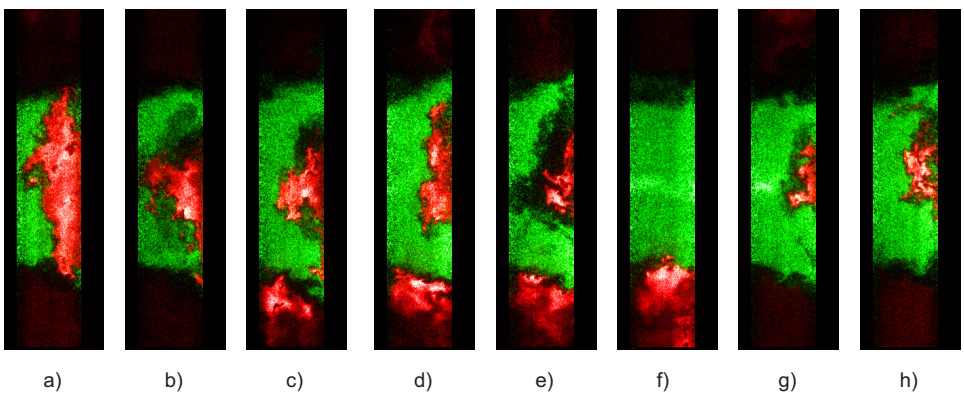

Figure 5.14: *Single-shot images of OH (red) and acetone (green) LIF signal distributions for different MFR, PFR and CFR settings in an industrial gas turbine burner. (a)-(b) MFR=100%, PFR=0% and CFR=0% (c)-(d) MFR=97%, PFR=3% and CFR=0% (e)-(f) MFR=94%, PFR=3% and CFR=3% (g)-(h) MFR=97%, PFR=0% and CFR=3%.*

the maximum intensity. The flame front, interpreted as the interface between the OH and acetone field, is strongly wrinkled, reflective of turbulent combustion. The effects of different values of PFR and CFR are clearly visible. The OH PLIF signal is found outside the main flame under operating conditions that involve the burning of pilot fuel, the main flame position being pushed downstream under operating conditions that involve the burning of central fuel, as compared with cases in which neither pilot fuel nor central fuel was burned.

Figure 5.15 shows the time-averaged acetone and OH PLIF radial signal distributions found at three different axial locations (10, 20 and 30 mm downstream), obtained under different sets of operating conditions. The acetone PLIF signal distribution is found to be symmetric around the central axis of the burner, Fig. 5.15a. Its shape is clearly affected by the PFR and CFR settings. Increasing the CFR value affects the radial shape of the distribution, the acetone PLIF signal distribution being pushed downstream, particularly in the core region. Increasing the PFR value results in the combustion reactions being shifted slightly upstream, both with and without the convention of central fuel. The shape of the OH PLIF distribution in the three axial positions suggests the flame to be conical in shape, the operating conditions which making use of the pilot fuel showing an asymmetric OH PLIF signal distribution. This is a surprising result, one also observed visually in the measurements. It was found that regions of strong OH PLIF signals occurred more frequently in the lower than in the upper parts of the images, see Fig. 5.14c-f. A possible explanation of this is that one of the 12 pilots was inactive during the measurements. The temperature close to the

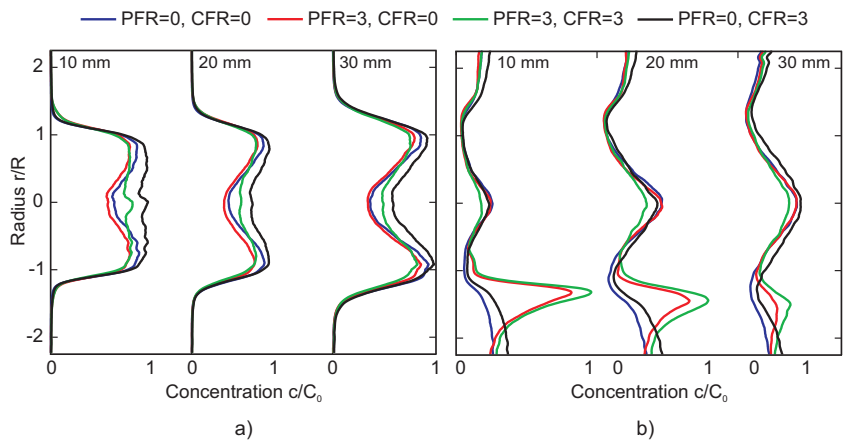

Figure 5.15: *(a) Time-averaged acetone (a) and OH (b) PLIF signal distributions along the radius at three different axial locations (10, 20 and 30 mm downstream) under different operating conditions. Blue line: MFR=100%, PFR=0% and CFR=0%, Red line: MFR=97%, PFR=3% and CFR=0%, Green line: MFR=94%, PFR=3% and CFR=3%, Black line: MFR=97%, PFR=0% and CFR=3%. Adapted from Paper VI.*

inactive pilot might be lower than at other pilots, this possibly affecting the combustion close to it. Since the inactive pilot was located close to the laser sheet, it is likely that it had an effect on the OH PLIF distribution, particular since this pilot was in the upper part of the burner. Another reason for the asymmetric OH PLIF distribution could be an asymmetry in the flow distribution of the cooling air in the thin channels around the burner. If such was the case, this could create areas in which the local additional air quenched the neighboring pilot flames, this occurring especially when the PFR values are small.

Parts of the experimental results were used for validation of both LES and RANS models. There are certain discrepancies between the experimental data and modeled data (see Paper VI), that could be due to the boundary conditions, to limited grid size or to the kinetic schemes in the models involved. In addition, the experimental data concern acetone PLIF signals and not acetone concentrations, the acetone PLIF signals not being compensated for possible by laser light absorption, signal trapping or quenching. Further information concerning the experiments and the LES and RANS models can found in Paper VI.

5.3.4 OH visualization in a natural gas/hydrogen fueled gas turbine burner

In the fourth measurement campaign, performed early in 2012, the natural gas fuel was mixed with differing amount of hydrogen, in view of hydrogen being a potential fuel for use in the future [4]. OH PLIF was employed for studying how the proportion of hydrogen involved affects the flame behavior of the burners in question. Figure 5.16 presents averaged images of the OH PLIF signal distribution for 30, 60 and 80 vol% hydrogen mixed with the natural gas. An averaged image obtained with use of natural gas alone as fuel is shown first, for purposes of comparison. The flow direction is from left to right in the images, the laser sheet propagating from bottom to top. With use of natural gas alone as fuel, the main flame takes a position downstream from the burner, see Fig. 5.16a. When hydrogen is added to the natural gas, the mean flame position is shifted towards the burner nozzle and eventually into the premixing tube, see Fig. 5.16b-d. This appears to quite likely be an effect of the increase in laminar flame speed and of interaction with turbulence when the natural gas is partly increased by hydrogen in the fuel. It was also observed that the flame begins to be attached to the burner outlet when the amount of hydrogen is increased, also when there is no pilot flame. The attachment of the flame to the burner outlet is unwanted, since it can lead to an increase in the temperature of the burner surface, which in turn could lead to the flame propagating upstream close to the wall, inside the premixing tube. It was also observed that the mean height of the flame in the combustion chamber was reduced when the amount of hydrogen was increased, due apparently to the shift of the flame upstream. There were also differences in signal intensity between the lower and upper parts of the averaged images. The size of these difference increased when the proportion of hydrogen in the fuel increased, this presumably being due to absorption caused by an increase in the amounts of OH radicals present. When the ratio of hydrogen to natural gas increases continuously, a limit is reached sooner or later, where the flame

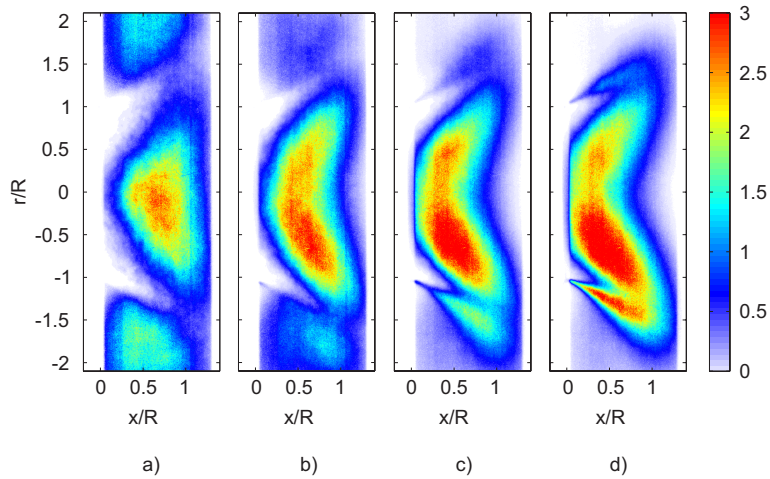

Figure 5.16: *Average OH PLIF signal distributions in an industrial gas turbine burner fueled by a natural gas/hydrogen mixture. (a) 100 vol% natural gas. (b) 70 vol% natural gas and 30 vol% hydrogen. (c) 40 vol% natural gas and 60 vol% hydrogen. (d) 20 vol% natural gas and 80 vol% hydrogen. The intensity scale of (a) and (b) is one third that of (c) and (d). The axes are normalized to the radius of the burner outlet. Unpublished data.*

speed becomes higher than the current gas velocity and flashback occurs. This limit is of critical importance, particularly when hydrogen is used as fuel. This limit was found to be at around 90 vol% hydrogen under the operating condition and the burner configuration employed. One should note, however, that these are only preliminary results.

5.4 Measurements in the HPVB (high-pressure vessel and burner)

There are usually considerable challenges to be met in the modeling combustion of commercially used fuels. One way of overcoming such problems is to use surrogate fuels, which are simplified representatives of actual fuels, in the modeling. Surrogate fuels can emulate the physical properties (vapor pressures) or combustion properties (laminar flame speed) of actual fuels sufficiently well for the results obtained to be relevant. Here, use of the HPVB makes it possible to isolate the impact of the fuel chemistry on the combustion behavior of fuels that are relevant, since it has the capability of burning vaporized liquid fuels under conditions of laminar diffusion flames and in partially premixed flames. In the present work, flame position and polyaromatic hydrocarbon (PAH) distributions in laminar partially premixed flames, as well as in laminar diffusion flames involving use of different surrogate fuels were visualized by use of OH PLIF and PAH PLIF. Liquid surrogate fuels such as n-heptane, n-decane and ethanol were studied, since these can be used as surrogates for gasoline, diesel and biofuels, respectively.

In addition, methane laminar diffusion flames, doped with small amounts of toluene or benzene, were studied in order to generate experimental data for the validation of a numerical model that could be used for modeling the conversion of tars during biomass gasification. Here, benzene and toluene are regarded as tar representatives. The results of the measurements serve as data base for the kinetic mechanisms being studied and as validation data for different CFD models. The n-heptane measurements are discussed in section 5.4.1, the methane measurements being discussed in section 5.4.2 and in Paper VII.

The optical experimental setup used for investigating the fuels in the HPVB, by means of both OH PLIF and of PAH PLIF is shown in Fig. 5.17. For measurements of OH PLIF, a measurement scheme similar to that used in the other measurement projects was employed, see section 5.1.2 for details. The 35 mm high vertical laser sheet was created by use of sheet-forming optics. For the PAH measurements, the fourth harmonic from a Nd:YAG laser, at 266 nm, was used. The same laser-sheet optics, ICCD camera and UV-lens were employed as for the OH PLIF measurements. The combination of a liquid dimethylformamide filter and a BG3 (Schott) filter was used to suppress laser scattering and to collect the fluorescence signals within the 300-500 nm range. When using 266 nm excitation, contributions from soot incandescence could be detected in the PAH PLIF fluorescence signal [63]. In order to distinguish these from one another, two subsequent measurements were carried out: prompt detection (the camera being synchronized with the laser pulse), which registers both PLIF

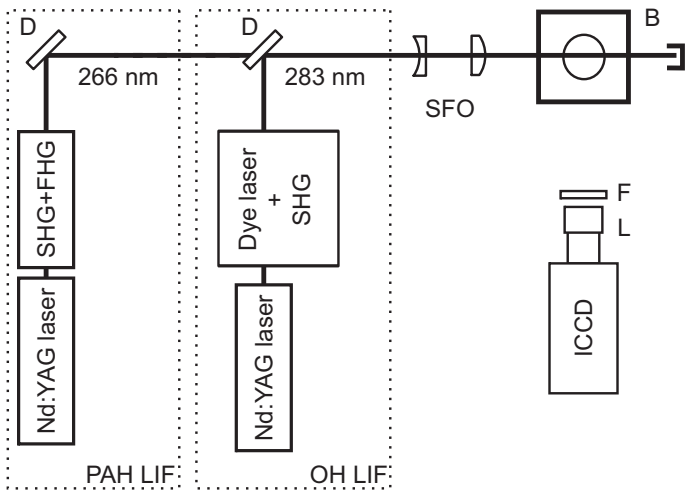

Figure 5.17: *Experimental setup used for the OH and PAH PLIF measurements in the HPVB. The abbreviations denote the following: D, dichroic mirror; SFO, sheet-forming optics; B, burner; L, camera lens; F, filter; ICCD, intensified CCD camera; SHG, second harmonic generation; FHG, fourth harmonic generation.*

and soot incandescence, and delayed detection (the camera being 50 ns after the laser pulse), which separates the PLIF signals from the soot incandescence signal. Delayed detection is a strategy used to locate regions in which the PAH PLIF signal is subjected to interference caused by soot incandescence.

5.4.1 Measurements in n-heptane/air flames

Qualitative measurements were made of the OH and PAH distributions in partially premixed n-heptane flames in the HPVB, the equivalence ratios being between ϕ=1.5 and ϕ=4 and the pressure 1 bar. Figure 5.18a shows the average OH PLIF signal distribution, the OH PLIF signal being found in the outer part of the flame where the temperature is high as a result of the combustion of fuel and PAHs. The average PAH PLIF signal distribution was surrounded by the PLIF signal from the OH distribution, see Fig. 5.18b. The PAH molecule, that were formed in the fuel-rich part and hot gas mixtures were oxidized in the combustion zone. At sufficiently high equivalence ratios, the PAH forms soot, which in turn is oxidized higher up in the flame. As already mentioned, contributions from both soot incandescence and PAH fluorescence were found in the PAH PLIF signal detected. Delayed detection of the PAH PLIF signal was employed to distinguish between PAH PLIF regions with and without contributions from

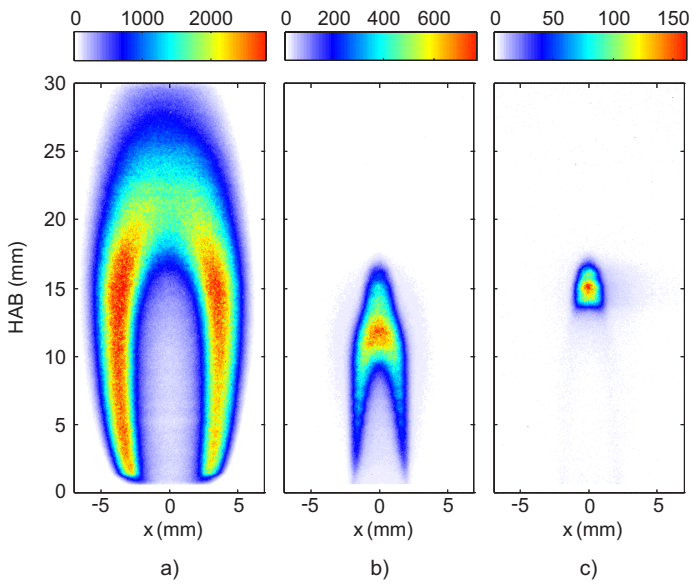

Figure 5.18: *Example of results from a partially premixed n-heptane flame at ϕ=3.7 and 1 bar. (a) Qualitative average OH PLIF signal distribution obtained. (b) Qualitative average PAH PLIF signal distribution obtained by use of prompt detection. (c) Qualitative average PAH PLIF signal distribution obtained by use of delayed detection. Unpublished data.*

soot incandescence. Figure 5.18c shows the PAH PLIF signals detected with a delay involved. As can be seen, the sharp structure at the top in Fig. 5.18b contains both PLIF signals from PAH molecules and LII from soot. This was also confirmed by laser-induced incandescence (LII) measurements, carried out after the PLIF measurements had been completed [64].

5.4.2 Measurements in methane/air flames

OH PLIF and PAH PLIF were applied to methane laminar diffusion flames doped with toluene and benzene, so as to generate experimental data for the validation of different numerical models. The dopants, toluene and benzene, are tar-model representatives. Tars, which are formed during biomass gasification, consist of polyaromatic hydrocarbons (PAH), the formation of which during the thermal decomposition of biomass cannot be avoided. It is important to have knowledge concerning their conversion, different numerical models relating to it having been developed. One example of a numerical model of this sort is the flamelet-generated manifold (FGM) reduction technique [65]. The aim of the work reported in Paper VII was to validate the FGM model on the basis of measurements of OH and PAH PLIF performed in doped diffusion methane flames.

The average OH PLIF signal distribution (left) and the OH mass fraction calculated by use of FGM (right) for the dopant-free flame are shown in Fig. 5.19a. The OH PLIF signal was found in the outer part of the flame, where the temperature was high as a result of combustion of fuel and PAHs. To be able to compare, the experimental data and the FGM data, both of these were normalized. The differences between the experimental data and the FGM data can be explained by the burner tip not being included in the FGM model, by its being difficult to match the correct boundary conditions in experiments involving coflow flames, and by the experimental data being OH PLIF signals and not OH mass fractions. Also, the fuel flow was preheated during the measurements, which could lead to deviations in the height of the flame. Figure 5.19b presents the measured averaged PAH PLIF signal distribution (left) and a summation of the calculated PAH mass fractions (right) obtained using the FGM model. PAH PLIF signals are found before the flame front on the fuel side, where the PAH molecules are formed, their later being oxidized in the combustion zone. The FGM model captures only the lowest part of the experimental profile. The differences in height can be due to only those PAH molecules containing up to three aromatic rings being modeled and to the PAH molecules with more than three aromatic rings being able to be detected in the experiments. The differences can also be due to the PAH fluorescence signals becoming red-shifted, i.e. shifted toward longer wavelengths, when the temperature is increased [66].

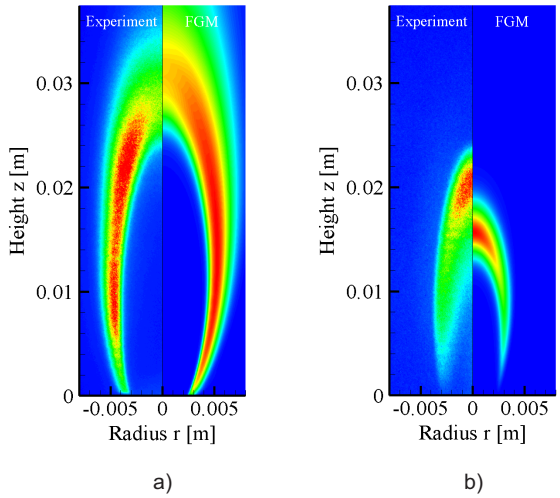

Figure 5.19: *Comparison of the experimental with the modeled results for a laminar methane/air diffusion flame. The color scheme is based on normalization of both the signal strength (experiment) and the species mass fractions (numerical model). (a) OH PLIF signals (left) and calculated OH mass fractions (right) (b) PAH PLIF signals (left) and calculated PAH mass fractions (right).*

When measurements on flames produced by fuels to which a dopant had been added were compared with measurements made on dopant-free flames, no effect of the OH PLIF signal distribution could be detected, but there was an increase in the PAH PLIF signals. Figure 5.20a shows the average PAH PLIF signal distribution obtained when toluene (2222 ppm) was used as a dopant. There, a strong PLIF signal can be observed close to burner tip, this being fluorescence of the unburned toluene, the toluene showing a strong absorption at 266 nm and a strong emission between 270 and 340 nm [16]. In addition, in some of the dopant flames a set of filters was employed making it possible to distinguish in qualitative terms between the smaller aromatic species (with 1-2 aromatic rings) and the larger ones (with 3 or more aromatic rings), i.e. between these showing characteristic fluorescence in the UV region and in the visible region, respectively [67]. The combination of a UG11 (Schott) filter and a WG320 (Schott) filter was used for the small aromatics and the combination of a GG420 (Schott) filter and a BG12 (Schott) filter for the larger aromatics [68]. The PLIF results obtained when the filter for small aromatic species was employed are shown in Fig. 5.20b. These experimental results were compared with the sum of all of the calculated species mass fractions obtained for species having a molar mass less than that of the 2-ring aromatic species naphthalene. The FGM model predicts strong PLIF signal to be obtained close to the burner tip, but there are difficulties in the use of the model to predict the PAH PLIF signals higher up in the flame. The results obtained with use of the filter for larger aro-

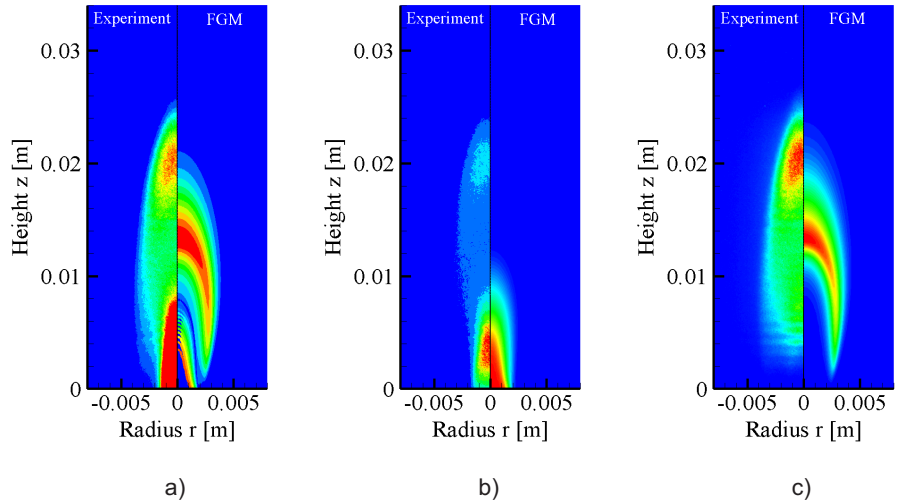

Figure 5.20: *Comparison between experimental results and modeled results for a laminar methane/air diffusion flame doped with 2222 ppm toluene. The color scheme is based on normalization of both the signal strength (experiment) and the species mass fractions (numerical model). (a) PAH PLIF signals (left) and calculated PAH mass fractions (right) (b) Filtered (small aromatic) PAH PLIF signals (left) and numerical results showing the mass fraction of the dopant C_7H_8 (right) (c) Filtered (large aromatic species) PAH PLIF signals (left) and numerical results showing the summed mass fractions for 3-ring species (right).*

matic species are shown in Fig. 5.20c. There, the PAH PLIF signal is compared with that obtained for model data involving the sum of those species mass fractions pertaining to 3-ring aromatic species. The FGM model also has certain difficulties here in predicting the position of the PAH PLIF signals. This can indicate that PAHs involving aromatic species containing more than 3 rings were also detected in the experiments. In line with this, it was observed that most of the PAH PLIF signals higher up in the flame originated from aromatic species containing 3 or more aromatic rings, cf. Fig. 5.20a-c. The experimental results indicate that the FGM model can be improved and be developed further by including aromatic species with more than 3 rings, since it appears that larger PAHs are relevant to the appearance of the flame. However, it should born in mind that the experimental results are not based on mass fractions, as the modeled results are. Further information concerning the experiments and the results obtained can be found in Paper VII.

In addition to the measurements pertaining to the doped methane flames, measurements were also performed in partially premixed methane flames in which the pressures involved were elevated. Although the use of HPVB allows studies of flames at pressures of up to 30 bar to be carried out, measurements only being performed here at pres-

sures of up to 6 bar, since the flame became unstable at higher pressures. Figure 5.21 shows examples of average OH PLIF signal distributions for partially premixed methane flames (ϕ=1.5) at 1 bar, 3 bar and 6 bar, respectively. As can be seen, the flame become smaller with an increase in pressure.

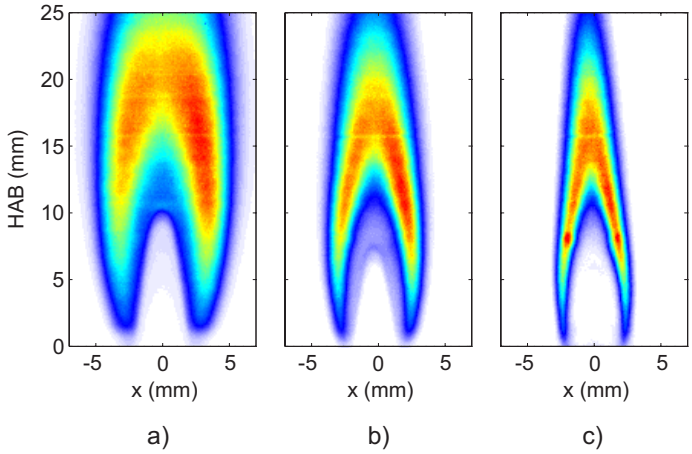

Figure 5.21: *(a) The average OH PLIF signal distribution for a partially premixed methane flame (ϕ=1.5) at 1 bar. (b) The average OH PLIF signal distribution for a partially premixed methane flame (ϕ=1.5) at 3 bar. (c) The average OH PLIF signal distribution for a partially premixed methane flame (ϕ=1.5) at 6 bar. Unpublished data.*

Chapter 6

Summary and outlook

To summarize, laser-based techniques were applied to different combustion devices related to gas turbine combustors for investigating them, and to improve in so far as possible knowledge of the combustion processes involved. Adequate knowledge of these combustion processes is highly important for being able to develop new gas turbines showing a high level of fuel efficiency and a low degree of pollutant species formation. Laser-based techniques make it possible to perform non-intrusive measurements with high spatial and temporal resolution. The measurements can also be species-specific and be performed in hostile combustion environments. A drawback that laser-based techniques have, however, is that optical access to the measurements volume is required. In this work, laser-based techniques were used for visualization of flame position, fuel distribution and flow fields. Measurements were performed in four different combustion devices, the main results obtained, as well as the outlook for further studies, being summarized below.

The Triple Annular Research Swirler (TARS) burner, which simulates the character of a gas turbine in terms of fuel injection and flame stabilization, is a good burner to use in studies of different combustion phenomena. Investigations of how different swirler configurations affect the flame and the flow dynamics have been carried out, along with studies of flashback under different operating conditions. Simultaneous OH PLIF, acetone PLIF and PIV were used to visualize flame position, fuel distribution and flow field, respectively. It was found that swirler configurations differ from one another in the effects they have, especially in terms of the amounts of unburnt fuel found in the central parts of the flame. The greater the swirl was, the less unburnt fuel was present there, due to the better air/fuel mixing that the swirl brought about. For flashback, the flame was found to become more sensitive to this when the equivalence ratio was increased. In order to achieve an increased understanding of the flame/flow interaction, temporally resolved measurements needs to be performed. Use of temporally resolved measurements makes it is possible to follow changes in structure and to investigate the flame/flow interactions, such as in the vicinity of lean blow-out and flashback, these being two types of unwanted events that can occur during normal gas

turbine combustion.

To study the mixing of fuel and air, as well as fuel vaporization, high-speed imaging of fuel distribution of Jet A and biojet was performed in a gas turbine pilot burner. Fuel PLIF was used to visualize the liquid and the gas phase of the fuel and Mie scattering to visualize the liquid phase of the fuel. It was possible, in studying high-speed image sequences, to identify and follow over time the development of large structures, the liquid phase region being found, as expected, to be close to the burner nozzle, the evaporated fuel spray cone from the injector being observed there. The fuel PLIF and Mie scattering measurements were not performed simultaneously, however, which would have been the ideal procedure. Simultaneous fuel PLIF and Mie scattering measurements need to be carried out since this provides valuable information regarding fuel atomization and fuel vaporization. Adequate knowledge of these processes is important in order to be able to optimize combustion and minimize emissions from gas turbines.

Several measurement campaigns were carried out on-site at Siemens in Finspång, where laser-induced fluorescence was applied to numerous industrial gas turbine burners in order to study their combustion characteristics. OH PLIF and acetone PLIF were employed for the visualization of flame position and fuel distribution in natural gas and natural gas/hydrogen fueled burners under different operating conditions. It was found that the flame was subjected to large fluctuations in the axial direction and that the flame front was strongly wrinkled, the latter indicating turbulent combustion. For the natural gas/hydrogen mixture, the flame began to propagate upstream into the premixing tube of the burner, its becoming more sensitive to flashback. In the investigations, part of the experimental data was used for the validation of two CFD models (LES and RANS). Further studies of the combustion characteristics of hydrogen, and also of other alternative fuels, would be of interest. Temporally resolved measurements are of strong interest as well. The long term goal, however, is to be able to perform measurements in a gas turbine at full load and under realistic operating conditions. Achieving this is very difficult due to limitations to the optical access which is possible, but use of an endoscope or a fiber-optical probe could be a solution to this. Lee and Santavicca [69, 70] have demonstrated the use of a LIF-based fiber-optical probe for point measurements of equivalence ratios, liquid fuel vaporization and fuel vapor concentrations in gas turbine combustors. Their probe consisted of two optical fibers: the one for guiding the laser to the measurement volume and the other for collection of the fluorescence signal. However, the use of probes that are inserted into the measurement volume can affect the flow and flame dynamics, endoscopes mounted in the wall of the combustion chamber sometimes being a better solution. Richter et al. [71] showed the possibility of obtaining 2-dimensional PLIF measurements in a non-firing direct injection spark ignition engine by use of an endoscope coupled to a CCD camera for the collection of fluorescence signals. Recently, Gessenhardt et al. [72] used endoscopes for 2-dimensional PLIF measurements in a running spark ignition engine. They employed two endoscopes: the one for creating the laser sheet and guiding it into the combustion chamber and the other for collection of the fluorescence signal. Even though the measurement volumes of interest are larger in gas turbine combustors than in internal combustion engines, the use of endoscopes for measurements in gas turbine combustors

is still possible. The laser sheet that is created can be guided into the combustor through the central fuel injector and the fluorescence signal be collected through an endoscope mounted on the wall of the combustor. The barrel distortion of the image caused by the lens system in the endoscope can be a problem, however, if a large measurement volume is to be imaged.

Laminar, partially premixed flames in a high-pressure vessel and burner (HPVB) were characterized by means of visualization of the flame position (OH PLIF) and of the polyaromatic hydrocarbon (PAH) distribution (PAH PLIF). Flames of both liquid (n-decane, n-heptane and ethanol) and gaseous (methane) fuels were studied at atmospheric pressure. For partially premixed n-heptane flames, the OH PLIF signal distribution was in the outer part of the flame surrounding the distribution from PAH PLIF. In laminar diffusion methane flames doped with benzene and toluene, OH PLIF and PAH PLIF were applied for the validation of numerical models. The dopants benzene and toluene were used here since they can represent tars, which are formed during biomass gasification. In addition, measurements were also performed at pressures of 3 bar and 6 bar, where both the flame and the reaction zone were smaller in size. While the measurements were being conducted, the burner was only able to produce stable flames of up to 6 bar, even though the burner can operate at pressures of up to 30 bar. Thus, obtaining other measurements, at 30 bar, of both premixed and non-premixed flames would be of strong interest from a gas turbine point of view. Gas turbines are usually operated under lean conditions. To be able to operate the HPVB under such lean conditions, it need to be re-designed, the burner diameter having to be increased for example.

Acknowledgements

During my years at the Division of Combustion Physics I have met and worked with a large number of people, both in Lund and in industrial collaborations. During my research I have met many friendly and helpful people, and I would like to express my appreciation to all of them, and to some of them in particular.

First of all, I would like to thank my main supervisor and the Head of Combustion Physics, *Professor Marcus Aldén*. I am grateful for the opportunity I was given to work in the field of laser-based combustion diagnostics and to participate in interesting research projects. I appreciate the support and confidence you have shown me during these years and that you always have found a time in your hectic schedule when there has been something I have wanted to discuss with you.

I would also like to acknowledge the support *Robert Collin* has provided me, the excellent supervisor that he is. *Robert* has done most of the day-to-day supervision of my thesis. Your support has been of great importance in the realization of this work, and I am truly grateful for that. I appreciate very much the time you have taken to help me with things when needed and for the time we spent together at Siemens during the measurement campaigns that were carried out successfully. I think, in addition, we have tried all the restaurants and pizzerias in Finspång.[1]

During the first two years of my work I shared an office with *Johan Zetterberg*. It was a pleasure to share the office with you, despite or because of your having spend most of your time in your other office. *Johan* is one of the few at the Division who share my passion for soccer and we have had endless discussions about games, results and players. After those first two years, I got a new roommate, *Zhihua Wang*. *Zhihua* was a guest researcher from Zhejiang University in China. It was a pleasure to share the office with you during your two years here in Lund. We had very enjoyable discussions about everything from the Chinese culture and politics to research. I am especially thankful for all your help with my trip in China and for your and *Yanqun Zhu's* hospitality when I visited Hangzhou. I congratulate you on your Professorship. Who knows, I may come and visit you again. After *Zhihua* went back to Zhejiang University, I got a new roommate, *Anna-Lena Sahlberg*. It has been very nice sharing the office with you.

I would like to express my appreciation to *Professor Per-Erik Bengtsson*. It has always been a pleasure talking with you, and you have always taken the time to answer my

[1] There are not that many restaurants and pizzerias in Finspång

questions. We have also worked out and conducted laboratory education together, which has been a pleasure.

Frederik Ossler, *Mattias Richter*, *Zhongshan Li*, *Joakim Bood*, *Henrik Bladh* and *Christian Brackmann* are acknowledged for the interesting discussions we have had and for your answering my questions regarding molecular physics, spectroscopy and physics in general, as well as your assistance on laser-related issues. I would like to direct special thanks to *Mattias* for your help in the transportation of laser equipment to Siemens and to *Christian* for your help with the laser system the night before I was to transport it to Siemens.

Billy Kaldvee, *Elias Kristensson*, *Johan Sjöholm*, *Jonathan Johnsson*, *Johannes Lindén*, *Ronald Whiddon*, *Christoph Knappe*, *Edouard Berrocal*, *Olof Johansson*, *Alexis Bohlin*, *Nils-Erik Olofsson*, *Andreas Ehn*, *David Sedarsky*, *Piero Iudiciani*, *Holger Grosshans*, *Eric Baudoin* and *Tobias Joelsson* have all been great friends both at and off from work and I am thankful to you all for that. I am very grateful for the interesting discussions we have had about both science-related and non-science-related topics. I would like to direct special thanks to *Jonathan* for answering my questions regarding MatLab so patiently, *Ronald* for the transportation of laser equipment to Siemens, and *Jonathan*, *Christoph*, *David* and *Nils-Erik* for being great travel partners during our trip in China. I also thank *Johannes*, *Billy*, *Christoph* and *Linda Vallenhag*, with whom I have endeavored to teach young students the Schlieren technique and to use thermocouples, among other things. You have all been very helpful and it has been a pleasure to work with you.

I would also like to thank *Sven-Inge Möller* for the time you have always taken to discuss or to explain research-related matters for me. I am very grateful for that. Also, we have had many interesting conversations about various music groups.

I am indebted to the administrators, *Minna Ramkull*, *Cecilia Bille*, *Eva Persson*, *Anneli Nilsson Ahlm*, *Sara Holmgren* and *Nina Mårtensson*. You have helped me with administrative and economic issues throughout my time here and you have been a great support to me throughout the work. I would like to direct special thanks to *Cecilia* for letting me borrow the cell phone charger and for the Christmas present. I would also like to thank the technicians *Susanne Dunér* and *Åke Johansson* for your help with computer and electronics-related issues.

Rutger Lorensson deserves credit for excellent support in designing and constructing all sorts of mechanical equipment needed for the experimental work, as well as for operating and maintaining the high-pressure combustion rig during the measurements I performed there. *Rutger*, I know you are playing in a famous rock band, New Rotics, so please let me know when you have your next live gig at stadsparken. I am waiting with eager anticipation.

I would also like to thank all currently and previously present persons from the Division not mentioned by name. You have all contributed to the friendly atmosphere at work, as well as during our numerous social activities.

I would like to thank the *Swedish Energy Agency* through the *Centre for Combustion Science and Technology*, *CECOST*, for the financial support.

A lot of the work has involved collaboration with people at the Division of Fluid

Mechanics, as well as people outside Lund University, including researchers from other universities and industrial sites. The close collaboration with Siemens Industrial Turbomachinery AB in Finspång has been very fruitful and every time I was at Siemens in Finspång I was received in a very positive and friendly way and I have been working with nice, friendly and helpful people there. I want especially to thank *Daniel Lörstad*, *Jenny Larfeldt*, *Annika Lindholm*, *Arne Irewall*, *Peter Magnusson*, *Thomas Larsson*, *Jonas Hylén* and *Anders Persson*. You have helped me with everything ranging from organizing the measurement projects, operating the combustion test rig and repairing a motor of a dye circulator pump. I would like to thank *Róbert-Zoltán Szász*, *Piero Iudiciani* and *Seyed Mohammad Hosseini* for our pleasant collaboration during the TARS experiments. *Robi*, thanks for proofreading a part of my thesis. I also want to thank *Professor Ephraim J. Gutmark* at the University of Cinncinati for our fruitful discussions during your visits in Lund. *Marcelo de Andrade Oliveira* and *Bo Li* are gratefully acknowledged for our pleasant collaboration during the HVPB experiments. *Marcelo*, I may come and visit you in Amsterdam.

I would like to take the opportunity as well to thank my great friends *Rebecca*, *Anna*, *Sebastian*, *Viktor*, *Maria*, *Adde* and *Josefin*. We have done so many fun and crazy things together, and thanks especially for your support during this last year. I will never forget that.

I would also like to thank my golf coach, *Magnus "Frasse" Pettersson*, for always making me feel welcome at the golf club when I have had time to play.

Finally, I would like to direct my deepest gratitude to my parents, *Barbro* and *Jan-Erik*, for your concern and endless support during my work, as well as in life generally. Without your encouragements I would not have made it so far. *Barbro*, even if you are not here to see me finish this, I know that you are proud.

References

[1] IEA. *Key World Energy Statistics 2011*. International Energy Agency, 2011.

[2] Turns, S.R. *An introduction to combustion; concepts and applications*. McGraw-Hill International Editions, Singapore, 2nd edn., 2000.

[3] IEA. *World Energy Outlook 2009*. International Energy Agency, 2009.

[4] Lefebvre, A.H. and Ballal, D.R. *Gas turbine combustion; alternative fuels and emissons*. CRC Press, Taylor & Francis Group, Boca Raton, FL, 3rd edn., 2010.

[5] Pope, S.B. *Turbulent flows*. Cambridge University Press, New York, 2000.

[6] Poinsot, T. and Veynante, D. *Theoretical and numerical combustion*. R.T. Edwards, Inc., Philadelphia, 2nd edn., 2005.

[7] Kohse-Höinghaus, K. and Jeffries, J.B. *Applied combustion diagnostics*. Taylor & Francis, New York, 2002.

[8] Eckbreth, A.C. *Laser diagnostics for combustion temperature and species*. Combustion Science and Technology Books Series Vol. 3, Gordon & Breach, Amsterdam, 2nd edn., 1996.

[9] Barlow, R.S., Dibble, R.W., and Lucht, R.P. *Simultaneous measurement of Raman scattering and laser-induced OH fluorescence in nonpremixed turbulent jet flames*. Optics Letters, **14**(5):263–265, 1989.

[10] Richter, M., Axelsson, B., Nyholm, K., and Aldén, M. *Real-time calibration of planar laser-induced fluorescence air-fuel ratio measurements in combustion environments using in situ Raman scattering*. Twenty-Seventh Symposium (International) on Combustion, **27**(1):51–57, 1998.

[11] Bergano, N.S., Jaanimagi, P.A., Salour, M.M., and Bechtel, J.H. *Picosecond laser-spectroscopy measurement of hydroxyl fluorescence lifetime in flames*. Optics Letters, **8**(8):443–445, 1983.

[12] Ehn, A., Johansson, O., Bood, J., Arvidsson, A. Li, B., and Aldén, M. *Fluorescence lifetime imaging in a flame*. Proceedings of the Combustion Institute, **33**(1):807–813, 2011.

[13] Kohse-Höinghaus, K. *Laser techniques for the quantitative detection of reactive intermediates in combustion systems*. Progress in Energy and Combustion Science, **20**(3):203–279, 1994.

[14] Daily, J.W. *Laser induced fluorescence spectroscopy in flames*. Progress in Energy and Combustion Science, **23**(2):133–199, 1997.

[15] Puri, R., Moser, M., Santoro, R.J., and Smyth, K.S. *Laser-induced fluorescence measurements of OH-concentrations in the oxidation region of laminar, hydrocarbon diffusion flames*. Twenty-Fourth Symposium (International) on Combustion, **24**(1):1015–1022, 1992.

[16] Schulz, C. and Sick, V. *Tracer-LIF diagnostics: quantitative measurement of fuel concentration, temperature and fuel/air ratio in practical combustion systems*. Progress in Energy and Combustion Science, **31**(1):75–121, 2005.

[17] Neij, H. *Development of Laser-Induced Fluorescence for Precombustion Diagnostics in Spark-Ignition Engines*. Doctoral Thesis, Lund University, Lund, 1998.

[18] Persson, H., Sjöholm, J., Kristensson, E., Johansson, B., Richter, M., and Aldén, M. *Study of fuel stratification on spark assisted compression ignition (SACI) combustion with ethanol using high speed fuel PLIF*. SAE Technical Paper 2008-01-2401, 2008.

[19] Kang, D.M., Fernandez, V., Ratner, A., and Culick, F.E.C. *Measurements of fuel mixture fraction oscillations of a turbulent jet non-premixed flame*. Combustion and Flame, **156**(1):214–220, 2009.

[20] Galley, D., Ducruix, S., Lacas, F., and Veynante, D. *Mixing and stabilization study of a partially premixed swirling flame using laser induced fluorescence*. Combustion and Flame, **158**(1):155–171, 2011.

[21] Hansen, A.D. and Lee, E.K.C. *Radiative and nonradiative transitions in the first excited singlet state of symmetrical methyl-substituted acetones**. The Journal of Chemical Physics, **62**(1):183–189, 1975.

[22] Yip, B., Miller, M.F., Lozano, A., and Hanson, R.K. *A combined OH/acetone planar laser-induced fluorescence imaging technique for visualizing combusting flows*. Experiments in Fluids, **17**(5):330–336, 1994.

[23] Grossmann, F., Monkhouse, P.B., Ridder, M., Sick, V., and Wolfrum, J. *Temperature and pressure dependences of the laser-induced fluorescence of gas-phase acetone and 3-pentanone*. Applied Physics B, **62**(3):249–253, 1996.

[24] Ossler, F. and Aldén, M. *Measurements of picosecond laser induced fluorescence from gas phase 3-pentanone and acetone: implications to combustion diagnostics*. Applied Physics B, **64**(4):493–502, 1997.

[25] Thurber, M.C., Grisch, F., Kirby, B.J., Votsmeier, M., and Hanson, R.K. *Measurements and modeling of acetone laser-induced fluorescence with implications for temperature-imaging diagnostics*. Applied Optics, **37**(21):4963–4978, 1998.

[26] Thurber, M.C. and Hanson, R.K. *Pressure and composition dependences of acetone laser-induced fluorescence with excitation at 248, 266, and 308 nm*. Applied Physics B, **69**(3):229–240, 1999.

[27] Löfström, C., Engström, J., Richter, M., Kaminski, C.F., Johansson, P., Nyholm, K., Hult, J., Nygren, J., and Aldén, M. *Feasibility studies and application of laser/optical diagnostics for characterisation of a practical low-emission gas turbine combustor*. ASME Turbo Expo Paper 2000-GT-0124, 2000.

[28] *Handbook of aviation fuel properties*. CRC Report No. 365, Coordinating Research Council, Inc (CRC), Alpharetta, GA, 3rd edn., 2004.

[29] Raffel, M., Willert, C.E., Wereley, S.T., and Kompenhans, J. *Particle image velocimetry; a practical guide*. Springer-Verlag, Berlin ; Heidelberg ; New York, 2nd edn., 2007.

[30] Sadanandan, R., Stöhr, M., and Meier, W. *Simultaneous OH-PLIF and PIV measurements in a gas turbine model combustor*. Applied Physics B, **90**(3-4):609–618, 2008.

[31] Petersson, P., Olofsson, J., Brackmann, C., Seyfried, H., Zetterberg, J., Richter, M., Aldén, M., Linne, M.A., Cheng, R.K., Nauert, A., Geyer, D., and Dreizler, A. *Simultaneous PIV/OH-PLIF, Rayleigh thermometry/OH-PLIF and stereo PIV measurements in a low-swirl flame*. Applied Optics, **46**(19):3928–3936, 2007.

[32] Adrian, R.J. *Particle-imaging techniques for experimental fluid mechanics*. Annual Review of Fluid Mechanics, **23**:261–304, 1991.

[33] Westerweel, J. *Fundamentals of digital particle image velocimetry*. Measurement Science and Technology, **8**(12):1379–1392, 1997.

[34] Svelto, O. and Hanna, D.C. *Principles of lasers*. Plenum Press, New York, 4th edn., 1998.

[35] Siegman, A.E. *Lasers*. University Science Books, Mill Valley, CA, 1986.

[36] Löfström, C., Kaaling, H., and Aldén, M. *Visualization of fuel distributions in premixed ducts in a low-emission gas turbine combustor using laser techniques*. Twenty-Sixth Symposium (International) on Combustion, **26**(2):2787–2793, 1996.

[37] Brackmann, C., Nygren, J., Bai, X., Li, Z.S., Bladh, H., Axelsson, B., Denbratt, I., Koopmans, L., Bengtsson, P.E., and Aldén, M. *Laser-induced fluorescence of formaldehyde in combustion using third harmonic Nd:YAG laser excitation*. Spectrochimica Acta Part A: Molecular and Biomolecular Spectroscopy, **59**(14):3347–3356, 2003.

[38] Bladh, H., Johnsson, J., and Bengtsson, P.E. *Influence of spatial laser energy distribution on evaluated soot particle sizes using two-colour laser-induced incandescence in a flat premixed ethylene/air flame*. Applied Physics B, **96**(4):645–656, 2009.

[39] Stopper, U., Aigner, M., Ax, H., Meier, W., Sadanandan, R., Stöhr, M., and Bonaldo, A. *PIV, 2D-LIF and 1D-Raman measurements of flow field, composition and temperature in premixed gas turbine flames*. Experimental Thermal and Fluid Science, **34**(3):396–403, 2010.

[40] Svanberg, S. *Atomic and molecular spectroscopy; basic aspects and practical applications*. Springer-Verlag, Berlin ; Heidelberg ; New York, 4th edn., 2004.

[41] Hult, J., Richter, M., Nygren, J., Aldén, M., Hultqvist, A., Christensen, M., and Johansson, B. *Application of a high-repetition-rate laser diagnostic system for single-cycle-resolved imaging in internal combustion engines*. Applied Optics, **41**(24):5002–5014, 2002.

[42] Walsh, P.P. and Fletcher, P. *Gas turbine performance*. Blackwell Science Ltd, Oxford, 2nd edn., 2004.

[43] Nair, S. and Lieuwen, T. *Near-blowoff dynamics of a bluff-body stabilized flame*. Journal of Propulsion and Power, **23**(2):421–427, 2007.

[44] Sommerer, Y., Galley, D., Poinsot, T., Ducruix, S., Lacas, F., and Veynante, D. *Large eddy simulation and experimental study of flashback and blow-off in a lean partially premixed swirled burner*. Journal of Turbulence, **5**(37), 2004.

[45] Schuller, T., Durox, D., and Candel, S. *Self-induced combustion oscillations of laminar premixed flames stabilized on annular burners*. Combustion and Flame, **135**(4):525–537, 2003.

[46] Lefebvre, A.H. *The role of fuel preparation in low-emission combustion*. Journal of Engineering for Gas Turbines and Power, **117**(4):617–654, 1995.

[47] Siemens Industrial Turbomachinery AB, Information about SGT-750. http://www.energy.siemens.com/co/en/power-generation/gas-turbines/sgt-750.htm.

[48] Siemens Industrial Turbomachinery AB, Information about SGT-800. http://www.energy.siemens.com/co/en/power-generation/gas-turbines/sgt-800.htm.

[49] Lindholm, A., Lörstad, D., Magnusson, P., Andersson, P., and Larsson, T. *Combustion stability and emissions in a lean premixed industrial gas turbine burner due to changes in the fuel profile*. ASME Turbo Expo Paper GT2009-59409, 2009.

[50] Seyfried, H., Brackmann, C., Lindholm, A., Linne, M., Barreras, F., and v. d. Bank, R. *Optical diagnostics applied to a gas turbine pilot burner*. AIAA Journal, **45**(11):2702–2709, 2007.

[51] v. d. Bank, R. and Schilling, T. *Development of an ultra-low NO_X LP(P) burner*. ASME Turbo Expo Paper GT2004-53341, 2004.

[52] de Andrade Oliveira, M.H. *Development and application of a laminar coflow burner for combustion studies at high pressure*. Doctoral Thesis, Eindhoven University of Technology, Eindhoven, 2012.

[53] Smooke, M.D., Lin, P., Lam, J.K., and Long, M.B. *Computational and experimental study of a laminar axisymmetric methane-air diffusion flame*. Twenty-Third Symposium (International) on Combustion, **23**(1):575–582, 1990.

[54] Smooke, M.D., Xu, Y., Zurn, R.M., Lin, P., Frank, J.H., and Long, M.B. *Computational and experimental study of OH and CH radicals in axisymmetric laminar diffusion flames*. Twenty-Fourth Symposium (International) on Combustion, **24**(1):813–821, 1992.

[55] Li, G. and Gutmark, E.J. *Effect of exhaust nozzle geometry on combustor flow field and combustion characteristics*. Proceedings of the Combustion Institute, **30**(2):2893–2901, 2005.

[56] Li, G. and Gutmark, E.J. *Boundary condition effects on nonreacting and reacting flows in a multiswirl combustor*. AIAA Journal, **44**(3):444–456, 2006.

[57] Fureby, C., Grinstein, F.F., Li, G., and Gutmark, E.J. *An experimental and computational study of a multi-swirl gas turbine combustor*. Proceedings of the Combustion Institute, **31**(2):3107–3114, 2007.

[58] Berkooz, G., Holmes, P., and Lumley, J.L. *The proper orthogonal decomposition in the analysis of turbulent flows*. Annual Review of Fluid Mechanics, **25**:539–575, 1993.

[59] Duwig, C. and Iudiciani, P. *Extended proper orthogonal decomposition for analysis of unsteady flames*. Flow, Turbulence and Combustion, **84**(1):25–47, 2010.

[60] Stöhr, M., Sadanandan, R., and Meier, W. *Phase-resolved characterization of vortex-flame interaction in a turbulent swirl flame*. Experiments in Fluids, **51**(4):1153–1167, 2011.

[61] Frank, J.H., Miller, M.F., and Allen, M.G. *Imaging of laser-induced fluorescence in a high-pressure combustor*. 37th AIAA Aerospace Sciences Meeting & Exhibit, Paper AIAA 99-0773, 1999.

[62] Siemens Industrial Turbomachinery AB, Information about SGT-700. http://www.energy.siemens.com/co/en/power-generation/gas-turbines/sgt-700.htm.

[63] Vander Wal, R.L., Jensen, K.A., and Choi, M.Y. *Simultaneous laser-induced emission of soot and polycyclic aromatic hydrocarbons within a gas-jet diffusion flame*. Combustion and Flame, **109**(3):399–414, 1997.

[64] Olofsson, N.E., Bladh, H., Johnsson, J., and Bengtsson, P.E. *Private communication*.

[65] van Oijen, J.A. and de Goey, L.P.H. *Modelling of premixed laminar flames using flamelet-generated manifolds*. Combustion Science and Technology, **161**(1):113–137, 2000.

[66] Ossler, F., Metz, T., and Aldén, M. *Picosecond laser-induced fluorescence from gas-phase polycyclic aromatic hydrocarbons at elevated temperatures. I. Cell measurements*. Applied Physics B, **72**(4):465–478, 2001.

[67] Beretta, F., D'Alessio, A., D'Orsi, A., and Minutolo, P. *U.V. and visible laser excited fluorescence from rich premixed and diffusion flames*. Combustion Science and Technology, **85**(1-6):455–470, 1992.

[68] Wu, J., Song, K.H., Litzinger, T., Lee, S.Y., Santoro, R., Linevsky, M., Colket, M., and Liscinsky, D. *Reduction of PAH and soot in premixed ethylene-air flames by addition of ethanol*. Combustion and Flame, **144**(4):675–687, 2006.

[69] Lee, J.G. and Santavicca, D.A. *Fibre-optic probe for laser-induced fluorescence measurements of the fuel-air distribution in a gas-turbine combustor*. Journal of Propulsion and Power, **13**(3):384–387, 1997.

[70] Lee, J.G. and Santavicca, D.A. *Fiber optic probe for primary zone fuel distribution measurements in actual liquid-fueled gas turbine combustors*. Proceedings of the SPIE Conference on Advanced Sensors and Monitors for Process Industries and the Environment, **3535**:167–175, 1998.

[71] Richter, M., Axelsson, B., and Aldén, M. *Engine diagnostics using laser induced fluorescence signals collected through an endoscopic detection system*. SAE Technical Paper 982465, 1998.

[72] Gessenhardt, C., Zimmermann, F., Schulz, C., Reichle, R., Pruss, C., and Osten, W. *Hybrid endoscopes for laser-based imaging diagnostics in IC engines*. SAE Technical Paper 2009-01-0655, 2009.

Summary of Papers

Paper 1: In this paper the TARS burner was investigated by means of laser diagnostics: OH PLIF to visualize the flame front, acetone PLIF to visualize the unburnt fuel and PIV to map the velocity field. Different swirler geometries, air flow rates and equivalence ratios were investigated. Measurements were performed in both in an axial direction and in a direction nearly perpendicular to axis of the cross-sectional planes. The work confirmed the considerable flexibility and the operability of the TARS burner, which enable both stable and repeatable flames under different operating conditions to be obtained. The stable flames were achieved without evidence of any vortex breakdown bubble, indicating that the flame can be stabilized dynamically through flame quenching and flame propagation. Proper orthogonal decomposition (POD) was performed in a highly unsteady case that was close to the lean blow-out limit. The results highlighted the rotational and helical dynamics that can actively contribute to instability of the flame.

I took part in planning the measurements and building the setup, and I participated in all the experimental work. I was the person mainly responsible for the PLIF measurements and Seyed Mohammad Hosseini was mainly responsible for the PIV measurements. Piero Iudiciani was responsible for post-processing of the data, for the POD analysis and for preparation of the manuscript as a whole, my writing the part dealing with PLIF.

Paper 2: In this paper the TARS burner was investigated experimentally in both confined and unconfined cases. The goal of this work was to promote more adequate use of post-processing techniques with the aim of extracting the dynamics of relevance from a given set of data. POD was applied to OH chemiluminescence data in the confined configuration. Two cases were considered: one in which the instability was continuous and one in which the flame was particularly unsteady and in which the phenomena were intermittent. The POD analysis succeeded in capturing the dynamics of flames undergoing thermo-acoustic instabilities. For the unconfined cases, OH PLIF measurements were performed in planes nearly perpendicular to the symmetry axis. An analysis of azimuthal modes, which are highly relevant to swirling flows, was carried out.

I took part in planning the measurements and building the setup, and I participated

in all the experimental work, except for the chemiluminescence measurements. I was responsible for the PLIF measurements. Piero Iudiciani was responsible for the data post-processing, the POD analysis and the preparation of the manuscript together with Christophe Duwig. I made no more than slight contributions to the manuscript.

Paper 3: Investigation of flame dynamics and flashback mechanisms in the TARS burner was investigated in this paper. A premixing tube was placed at the exit of the burner and simultaneous OH PLIF for flame front visualization and PIV for velocity field mapping were employed studying flow and flame dynamics during the transition from flame stabilization downstream from the premixing tube to flame flashback in the premixing tube. A variety of statistical evaluation methods, such as PDF of the axial velocity, the mean velocity field and the average OH distributions were performed on the data so as to obtain a better understanding of the flame stabilization mechanisms involved. In addition, POD analysis of the PIV and PLIF data was performed so as to reveal the different modes that characterize the dynamics of the flame.

I took part in planning the measurements and building the setup, and I participated in all of the experimental work. I was mainly responsible for the PLIF measurements and the PLIF data post-processing, and Seyed Mohammad Hosseini was mainly responsible for the PIV measurements, performed the PIV data post-processing and the POD analysis. Seyed Mohammad Hosseini was responsible for preparation of the manuscript as a whole, my writing the part dealing with PLIF.

Paper 4: In this note, several laser diagnostic techniques were applied to a gas turbine pilot burner. The measurements, carried out in the high-pressure combustion facility at Lund University, involved high-speed fuel visualization using PLIF and Mie scattering as well as flame front visualization using OH PLIF. A pressure-swirl atomizer fuel injector surrounded by a coflow was used during the tests, two different fuels, Jet A and biojet, being investigated. The aim was to examine the possibilities of performing laser diagnostics using these two fuels under different operating conditions and the challenges to be overcome in connection with this. In addition, the effects for Jet A of laser absorption with use of 266 nm excitation, which has been a problem in various earlier studies, was investigated. It was observed that the absorption effect can be avoided by using longer excitation wavelengths.

I took part in planning the measurements and in building the laser setup, and I participated in all the experimental work. I performed the data post-processing and was responsible for preparation of the manuscript.

Paper 5: In this paper, laser diagnostics was applied to different industrial gas turbine burners with the aim of better understanding the flow and flame dynamics involved. The combustion characteristics of the different burners were examined by simultaneous use of OH and acetone PLIF. The results showed there to be considerable fluctuation in the axial direction and the flame front to be highly wrinkled.

The laser diagnostics were complemented by LES and RANS simulation, which were validated against the experimental data. The LES results indicated the fuel distribution upstream from the flame to have significant effects on the flame dynamics.

I took part in planning the laser diagnostic measurements and building the laser setup, and I participated in all the experimental work. Robert Collin was responsible for the data post-processing and Niklas Alin and Christer Fureby performed the LES simulations. Annika Lindholm was responsible for maintenance and operation of the combustion rig. Daniel Lörstad performed the RANS simulations and was responsible for preparation of the manuscript. I made a small contribution to the manuscript.

Paper 6: In this paper, laser diagnostics was applied to different industrial gas turbine burners in order to obtain a better understanding of the mixing process and the flame dynamics of the burners. The combustion characteristics of the different burners were studied using OH and acetone PLIF simultaneously. The experimental data were used to validate RANS and LES simulations. Many different operating conditions were investigated, including operating conditions with and without pilot flames. The measurements revealed large fluctuations in the flame regions and reactions were found to occur further upstream under operating conditions involving use of pilot flames than under operating conditions without use of pilot flames.

I took part in planning the laser diagnostic measurements and in building the laser setup, and I participated in the experimental work. I was main responsible for the data post-processing and Ekaterina Fedina and Christer Fureby performed the LES simulations. Annika Lindholm was responsible for maintenance and operation of the combustion rig and Daniel Lörstad and Darioush Gohari Barhaghi performed the RANS simulations. Alessio Bonaldo conducted the water test rig measurements. Daniel Lörstad was responsible for preparation of the manuscript, my writing a small contribution to it.

Paper 7: In this paper, the OH PLIF and PLIF of polyaromatic hydrocarbons (PAH) were applied to toluene and benzene doped laminar diffusion methane flames. The dopants, toluene and benzene, are tar-model representatives. Tars, which are formed during biomass gasification, consist of PAHs, its being impossible to avoid their formation during the thermal decomposition of biomass. One example of a numerical model that can generate knowledge concerning the conversion involved is the flamelet-generated manifold (FGM) model, which was validated against the PLIF results. The FGM model was found able to capture the major flame characteristics typical of PAH formation in laminar diffusion flames. Also, a set of filters was used to be able to distinguish qualitatively between the small (1-2 ring) and the larger (3 or more ring) aromatic species.

I took part in planning the measurements and building the laser setup, and I had the main responsibility for the diagnostic measurements together with Bo Li. I performed the data post-processing and Liselotte Verhoeven performed the FGM simulations. Marcelo

de Andrade Oliveira was responsible for maintenance and operation of the burner. Liselotte Verhoeven was responsible for preparation of the manuscript, of which I wrote the PLIF part.